



Processing methodology for the ITS_LIVE Sentinel-1 ice velocity products

Yang Lei¹, Alex S. Gardner², and Piyush Agram¹

¹Division of Geological and Planetary Science, California Institute of Technology, Pasadena, CA 91125, USA

²Jet Propulsion Laboratory, California Institute of Technology, Pasadena, CA 91109, USA

Correspondence: Yang Lei (ylei@caltech.edu)

Received: 2 November 2021 – Discussion started: 14 December 2021

Revised: 22 September 2022 – Accepted: 26 September 2022 – Published: 22 November 2022

Abstract. The NASA MEaSUREs Inter-mission Time Series of Land Ice Velocity and Elevation (ITS_LIVE) project seeks to accelerate understanding of critical glaciers and ice sheet processes by providing researchers with global, low-latency, comprehensive and state of the art records of surface velocities and elevations as observed from space. Here we describe the image-pair ice velocity product and processing methodology for ESA Sentinel-1 radar data. We demonstrate improvements to the core processing algorithm for dense offset tracking, “*autoRIFT*”, that provide finer resolution (120 m instead of the previous 240 m used for version 1) and higher accuracy (20 % to 50 % improvement) data products with significantly enhanced computational efficiency (>2 orders of magnitude) when compared to earlier versions and the state of the art “dense ampcor” routine in the JPL ISCE software. In particular, the disparity filter is upgraded for handling finer grid resolution with overlapping search chip sizes, and the oversampling ratio in the subpixel cross-correlation estimation is adaptively determined for Sentinel-1 data by matching the precision of the measured displacement based on the search chip size used. A novel calibration is applied to the data to correct for Sentinel-1A/B subswath and full-swath dependent geolocation biases caused by systematic issues with the instruments. Sentinel-1 C-band images are affected by variations in the total electron content of the ionosphere that results in large velocity errors in the azimuth (along-track) direction. To reduce these effects, slant range (line of sight or LOS) velocities are used and accompanied by LOS parameters that support map coordinate (x/y) velocity inversion from ascending and descending slant range offset measurements, as derived from two image pairs. After the proposed correction of ionosphere errors, the uncertainties in velocities are reduced by 9 %–61 %. We further validate the ITS_LIVE Version 2 Sentinel-1 image-pair products, with 6-year time series composed of thousands of epochs, over three typical test sites covering the globe: the Jakobshavn Isbræ Glacier of Greenland, Pine Island Glacier of the Antarctic, and Malaspina Glacier of Alaska. By comparing with other similar products (PROMICE, FAU, and MEaSUREs Annual Antarctic Ice Velocity Map products), as well as other ITS_LIVE version 2 products from Landsat-8 and Sentinel-2 data, we find an overall variation between products around 100 m yr^{-1} over fast-flowing glacier outlets, where both mean velocity and variation are on the order of km yr^{-1} , and increases up to $300\text{--}500 \text{ m yr}^{-1}$ (3 %–6 %) for the fastest Jakobshavn Isbræ Glacier. The velocity magnitude uncertainty of the ITS_LIVE Sentinel-1 products is calculated to be uniformly distributed around 60 m yr^{-1} for the three test regions investigated. The described product and methods comprise the MEaSUREs ITS_LIVE Sentinel-1 Image-Pair Glacier and Ice Sheet Surface Velocities: version 2 (DOI: <https://doi.org/10.5067/0506KQLS6512>, Lei et al., 2022).

1 Introduction

As the planet warms in response to increased concentrations of greenhouse gases in the atmosphere, glaciers and ice sheets are losing more mass to the world's oceans, leading to accelerated rates of sea level rise (IPCC AR6, 2021). Glaciers and ice sheets are losing mass through both accelerated melting and solid ice discharge into the ocean via enhanced flow. How glacier and ice sheet flow will change in the future is one of the largest uncertainties in projections of sea level change. Ice flow velocity is a critical constraint for determining ice discharge (Gardner et al., 2018), modeling ice dynamics with numerical simulations (Farinotti et al., 2019), understanding the short-term and long-term ice flow dynamic variation (e.g., seasonal and/or tidal; Minchew et al., 2017; Greene et al., 2020) as well as calculating mass balance budgets (e.g., Bamber and Rivera, 2007; Minowa et al., 2021). Tracking of features in repeat satellite imagery provides a vantage point for measuring ice motion over continental scales (Bindshadler and Scambos, 1991; Frolich and Doake, 1998), providing insights into the processes that drive large-scale changes in flow. Surface velocities have been successfully derived from both optical and radar imagery including NASA's Landsat 4/5/6/7/8 (Fahnestock et al., 2016; Gardner et al., 2018), ESA's Sentinel-1 (Nagler et al., 2015; Andersen et al., 2020; Friedl et al., 2021; Solgaard et al., 2021) and Sentinel-2 (Kääb et al., 2016; Nagy and Andreassen, 2019), DLR's TerraSAR-X and TanDEM-X (Joughin et al., 2010) and through multi-mission synthesis (Miles et al., 2017; Mouginito et al., 2017a; Derkacheva et al., 2020).

Surface velocities can be derived from pairs of radar images using multiple techniques and programs, which have been cross-compared in a comprehensive way by carefully setting up the programs and coordinating with various groups worldwide (Boncori et al., 2018). In general, four different approaches have been shown to be capable of measuring surface velocities from radar and/or optical satellite data, i.e., synthetic aperture radar interferometry (InSAR; Goldstein et al., 1993), multi-aperture SAR interferometry (MAI; Borch and Zebker, 2006), incoherent offset-tracking (amplitude only; Gray et al., 1998), and coherent offset-tracking (amplitude and phase; Joughin, 2002). Among them, the most accurate technique (i.e., cm level for Sentinel-1) is InSAR that is highly sensitive to measure changes in range from repeat-pass observations (Joughin et al., 1995; Rignot et al., 1995; Gray et al., 1998; Joughin et al., 1998, 1999; Michel and Rignot, 1999; Yu et al., 2010; Gourmelen et al., 2011; Mouginito et al., 2019a). MAI is less widely used than the conventional (or differential) InSAR technique, because it is capable of measuring the azimuth velocity component only, which is thus more subject to the large velocity errors in the azimuth (along-track) direction that are due to the ionosphere effects in SAR processing and temporal decorrelation (Boncori et al., 2018). However, interferometry can be prob-

lematic over fast-flowing ice and/or areas where snow accumulation and melting occur due to rapid temporal decorrelation. In contrast, offset tracking (amplitude only; incoherent) or speckle tracking (amplitude and phase; coherent) have been predominantly used in tracking both along-track and line of sight (LOS) ice motion as it is less sensitive to phase unwrapping errors and temporal decorrelation (Fahnestock et al., 1993; Strozzi et al., 2002; de Lange et al., 2007; Strozzi et al., 2008; Nagler et al., 2012; Riveros et al., 2013; Fahnestock et al., 2016; Mouginito et al., 2017a; Kusk et al., 2018). As Boncori et al. (2018) showed, it is not yet convincing that the coherent offset-tracking method provides essentially more accurate results than the incoherent counterpart by sacrificing half of the efficiency (two times the runtime).

Besides regional attempts for generating ice flow maps, such as over high-mountain glaciers (Dehecq et al., 2015; Millan et al., 2019), several satellites derived large-scale operational ice velocity mappings are released annually (Nagler et al., 2015; Mouginito et al., 2019b; Joughin, 2020a) or more frequently (Joughin, 2020b; Gardner et al., 2019; Solgaard et al., 2021). Among these efforts, the NASA MEASUREs project Inter-mission Time Series of Land Ice Velocity and Elevation (ITS_LIVE) releases ice velocity products, i.e., (1) image-pair granules (without time averaging), (2) datacubes (time series of image-pair results) and (3) regional mosaics (averaged both spatially and temporally) with global coverage using temporally dense multi-sensor observations from both optical (Landsat 4/5/6/7/8 and Sentinel-2) and SAR (Sentinel-1) satellite data (Gardner et al., 2018). Other similar products of regional and/or global ice velocities have also been released, such as the Programme for Monitoring of the Greenland Ice Sheet (PROMICE) ice velocity product (Solgaard and Kusk, 2021) that releases temporally (24 d) averaged velocity mosaics over the Greenland Ice Sheet as well as the global products released by Friedrich Alexander University (FAU) that include image-pair (without time averaging) products, monthly and annual mosaics (Friedl et al., 2021). Furthermore, both products of PROMICE and FAU are generated purely using the Sentinel-1 SAR dataset via the offset tracking method, similar to our ITS_LIVE Version 2 Sentinel-1 products, which will then be cross-validated later in this work by comparing with PROMICE and FAU in various regions of the globe. The specifics of all three Sentinel-1-based data products (PROMICE, FAU and ITS_LIVE) are summarized in Table 1. As described by Lei et al. (2021a), the core processing algorithm of the ITS_LIVE project utilizes the combination of a precise geocoding module “*Geogrid*” and an efficient offset tracking module “*autoRIFT*” (autonomous repeat image feature tracking), both of which are open source (<https://github.com/nasa-jpl/autoRIFT>, last access: 1 March 2022) and have been integrated to NASA/JPL's InSAR Scientific Computing Environment (ISCE) software (<https://github.com/isce-framework/isce2>, last access: 1 March 2022).

Table 1. Sentinel-1 based data product specifics of PROMICE, FAU and ITS_LIVE.

Data product	Temporal resolution	Spatial resolution	Period	Method	Uncertainty*	Global/regional
PROMICE	24 d (temporally averaged)	Grid spacing 500 m (effective resolution: 800–900 m)	2016–present	Normalized cross correlation	20–27 m yr ⁻¹ (with in situ GPS) and 8–12 m yr ⁻¹ (over stable ground)	Greenland only
FAU (image-pair product)	6–12 d (no temporal averaging)	Grid spacing 200 m (effective resolution: 800–900 m)	2016–present	Normalized cross correlation	14.6 m yr ⁻¹ (with TerraSAR-X) and 87.6 m yr ⁻¹ (with Landsat-8)	Global
ITS_LIVE (image-pair product)	6–12 d (no temporal averaging)	Grid spacing 120 m (effective resolution: 240–1920 m)	2016–present	Normalized cross correlation	50–70 m yr ⁻¹ (over rocks and stationary surfaces)	Global

* assessed accuracy is highly dependent on target surface characteristics, magnitude and orientation of flow, and total electron content.

In this work we focus on the ITS_LIVE processing of the C-band Sentinel-1A/B radar data. Specifically, we focus on the processing of the terrain observation with progressive scan (TOPS) mode of the interferometric wide swath (IW) SAR observations (De Zan and Guarnieri, 2006; Prats-Iraola et al., 2015; Miranda et al., 2017; Schubert et al., 2017). This mode enables surface imaging with a 3.7 m ground range and 15.6 m azimuth resolution with a repeat cycle of 6 d between A and B satellites over polar regions and some other key areas of the world. The SAR imagery has qualities that are highly valuable for imaging of polar glaciers and ice sheets as the instrument is not obscured by cloud or limited by solar illumination. In Sect. 2.1, we provide an overview of the MEaSURES ITS_LIVE Sentinel-1 Image-Pair Glacier and Ice Sheet Surface Velocities: Version 2, on which the ITS_LIVE global ice velocity mosaics will be based. For illustration purposes, we show examples of several Sentinel-1 image pairs collected over Greenland (Lei et al., 2021b), and demonstrate several recent improvements to *autoRIFT* providing finer resolution, improved accuracy, and increased processing efficiency. In Sect. 2.2 we discuss the adoption of a 120 m regularly spaced output grid (previously a 240 m grid was used) with 50 % overlap in search chips and a modified normalized displacement coherence (NDC) filter. In Sect. 2.3 we discuss using a chip size-dependent subpixel oversampling ratio that improves subpixel accuracy while retaining computational efficiency. In Sect. 2.4 we present a runtime comparison between *autoRIFT* and the ISCE software default dense feature tracking algorithm, “dense amp-cor”. In Sect. 3 we discuss approaches to minimize systematic geolocation biases (Sect. 3.1) and effects of ionosphere disturbance (Sect. 3.2). In Sect. 4, we further validate the globally available ITS_LIVE Sentinel-1 image-pair products over three typical test sites: the Jakobshavn Isbræ Glacier of Greenland (Sect. 4.1), Pine Island Glacier of the Antarctic (Sect. 4.2), and Malaspina Glacier of Alaska (Sect. 4.3), by comparing with other similar products (PROMICE, FAU and other MEaSURES products) as well as other ITS_LIVE Ver-

sion 2 products from optical sensors (Landsat-8 and Sentinel-2) available in each region. A summary of the work is provided in Sect. 5.

2 ITS_LIVE Sentinel-1 image-pair product description and processing chain

In this section we provide a high-level overview of the ITS_LIVE Sentinel-1 image-pair product and the core processing algorithms. Both inputs to and outputs from the processing chain are demonstrated for a set of test data collected over Greenland. We then discuss two improvements to the *autoRIFT* processing chain that are exploited for Version 2 processing of the Sentinel-1 data.

2.1 Product and methodology overview

2.1.1 Input dataset

ITS_LIVE Sentinel-1 processing chain inputs and outputs are provided in Table 2.

Examples of input data for Greenland are illustrated in Fig. 1. In Fig. 1a, we demonstrate the magnitude of reference velocity from the 20-year ice-sheet-wide velocity mosaic (Joughin et al., 2010, 2016, 2017) derived from the synthesis of SAR/InSAR data and Landsat-8 optical imagery. In ITS_LIVE processing, both the x and y components of the reference velocity are used to center the downstream search routine. The three red rectangles in Fig. 1 show the locations used for demonstration and validation of the algorithms. The list of 21 Sentinel-1 image pairs used for validation is provided in Table 3 (Lei et al., 2021b). In Fig. 1b, we show the GIMP digital elevation model (DEM) for the Greenland Ice Sheet (Howat et al., 2014, 2015), which is used in this work for illustration purposes only. Note for the global processing, we considered various DEMs with different resolutions, e.g., Arctic DEM, REMA DEM, TanDEM-X DEM, Copernicus DEM, and NASADEM, and found the Copernicus DEM with global coverage at 30 m resolution (GLO-30) is the best

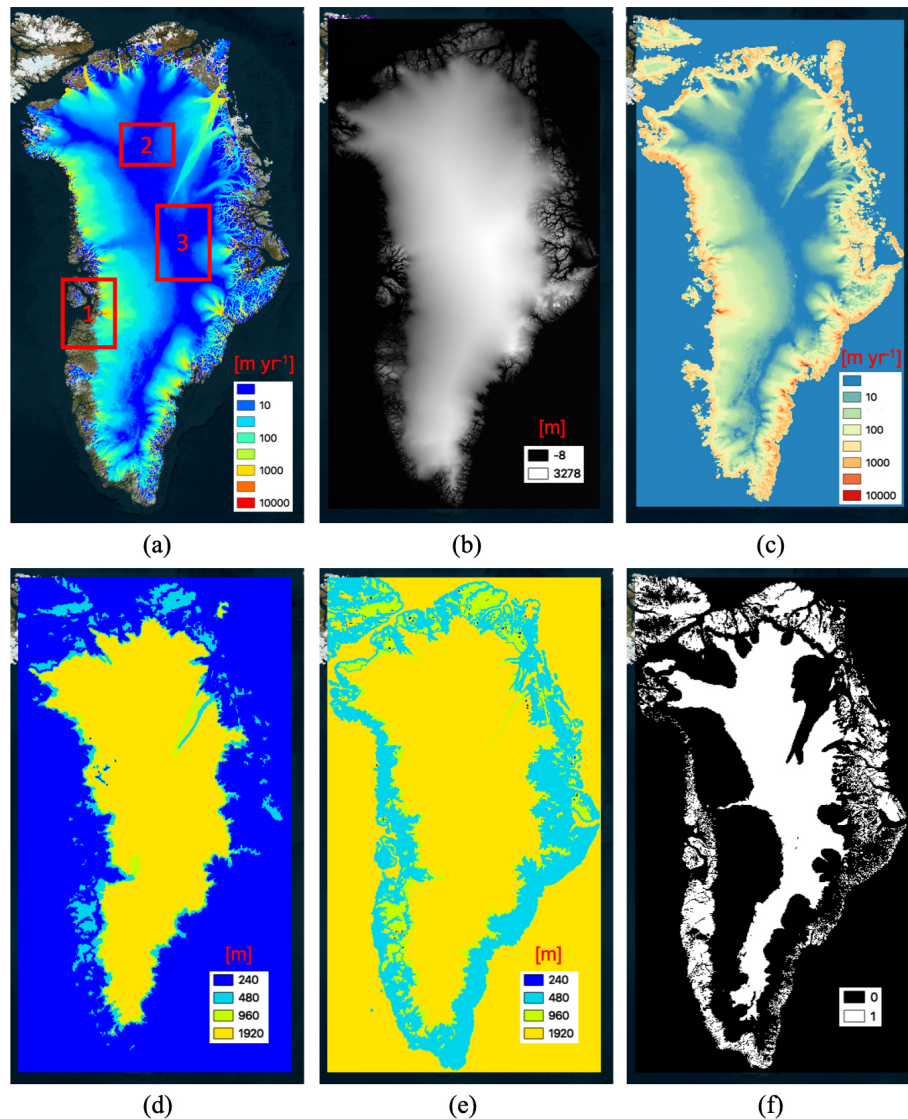


Figure 1. Input to the Sentinel-1 processing chain: (a) reference velocity magnitude with test sites shown as red rectangles, (b) elevation, (c) search limit in x , (d) minimum chip size, (e) maximum chip size, (f) stable surface mask that is defined as ice-free terrain or areas having a reference velocity $< 15 \text{ m yr}^{-1}$.

available large-scale DEM, which was also baselined for the NASA-ISRO NISAR mission after extensive analysis. With this analysis, it was found that DEMs with varying resolutions have negligible effects on the resulting offset tracking velocities given the grid spacing of 120 m used. Geolocation accuracy is, however, slightly more sensitive to the DEM resolution and accuracy. The DEM and its derivatives with respect to x and y directions, are all used to map between pixel index and displacement in radar range/azimuth coordinates and geolocation and surface velocity in map-projected Cartesian coordinates (northings/eastings). Note with a different DEM, the offset tracking estimates in radar coordinates (slant range/azimuth) are relatively insensitive to DEM errors, e.g., a DEM change or error of a few 10's of meters leads to pixel

misregistration in the order of 0.001 pixels. However, the DEM-derived surface slopes that are used in mapping between radar viewing geometry and the map-projected coordinate system are sensitive to the DEM error. Therefore, the map-projected velocity estimates tend to be affected by the DEM slope error (e.g., over regions with high topographic relief). The search limit is shown in Fig. 1c, which constrains the size of the search window and spatially varies with the reference velocity and proximity to the ocean. A search limit of zero indicates that no offset search should be conducted. Figure 1d and e are the minimum and maximum allowable chip sizes. The *autoRIFT* will cycle from the minimum to the maximum chip size until a “valid” offset is found (i.e., passing the NDC filter based on the derived pixel displacement

Table 2. Input and output data for the MEaSURES ITS_LIVE Sentinel-1 Image-Pair Glacier and Ice Sheet Surface Velocities: Version 2 processing chain, x and y are directions in map coordinates. Each output variable is accompanied by variable specific metadata.

Input	Sentinel-1 image pair Elevation [m above WGS84 ellipsoid] Topographic slopes in x and y [m m^{-1}] Reference velocity in x and y [m yr^{-1}] Search limit in x and y [m yr^{-1}] Minimum chip size in x and y [m] Maximum chip size in x and y [m] Stable surface mask [binary]
Output	v_x [int16]: velocity in x [m yr^{-1}] v_y [int16]: velocity in y [m yr^{-1}] v [int16]: velocity magnitude [m yr^{-1}] v_error [int16]: velocity magnitude error [m yr^{-1}] v_r [int16]: slant range (LOS) velocity [m yr^{-1}] v_a [int16]: azimuth (along-track) velocity [m yr^{-1}] M11 [int16]: velocity conversion matrix element (1st row, 1st column) M12 [int16]: velocity conversion matrix element (1st row, 2nd column) chip_size_height [uint16]: height (along azimuth) of chip [m] chip_size_width [uint16]: width (along range) of chip [m] interp_mask [uint8]: interpolation flag, 0 = measured, 1 = interpolated [binary] img_pair_info [char]: image-pair metadata

similarity with adjacent chips; as discussed in Sect. 2.2), returning the finest achievable resolution within the specified limits. Here we specify smaller chip sizes for fast-flowing glaciers (lower accuracy but higher spatial resolution) along the margin of Greenland and larger chip sizes (higher accuracy with lower resolution) for the interior regions where gradients in velocity are low (Fig. 1d, e). Figure 1f shows the stable surface mask that is defined as ice-free terrain or areas having a reference velocity $< 15 \text{ m yr}^{-1}$ and is used for calibration of the velocity fields.

As Fig. 1 shows, the above inputs of DEM and reference velocities are specifically chosen for the Greenland Ice Sheet and for illustration purposes only. For the global processing, including the Arctic, Antarctic and all the other areas of the world, e.g., high mountain glaciers, we use the Copernicus DEM GLO-30 (<https://spacedata.copernicus.eu/web/cscda/dataset-details?articleId=394198>, last access: 1 March 2022) and ITS_LIVE Version 1 Landsat-derived velocity mosaics (<https://its-live.jpl.nasa.gov>, last access: 1 March 2022) as the reference velocities for deriving all our Version 2 ITS_LIVE products. For the Greenland and Antarctic ice sheets, ITS_LIVE Version 1 Landsat-derived velocity mosaics are combined with MEaSURES Greenland Ice Sheet Velocity Map from InSAR Data V002 (Joughin et al., 2010, 2015) and MEaSURES InSAR-Based Antarctica Ice Velocity Map, Version 2 (Mouginot et al., 2012; Rignot et al., 2017), respectively. All inputs were provided on a common 120 m grid. The NSIDC Sea Ice Polar Stereographic North projection (EPSG code 3413) is used for all areas north of 55° N latitude. For areas south of 56° S lati-

tude the Antarctic Polar Stereographic South (EPSG 3031) projection is used. For the rest of the world we use local universal transverse mercator (UTM) projections. For all map projections, a constant grid posting of 120 m is used to enhance the product resolution (by 50 %) while keeping computational demands within reason. A 240 m posting was used for Version 1.0 of the ITS_LIVE image-pair products.

2.1.2 ITS_LIVE Sentinel-1 image-pair data product

Figure 2 shows the spatial coverage of the ITS_LIVE Version 2 Sentinel-1 image-pair velocity product (<https://doi.org/10.5067/0506KQLS6512>, Lei et al., 2022). The dataset can currently be queried using the ITS_LIVE data portal (<https://nsidc.org/apps/itslive/>, last access: 1 March 2022) or by using the ITS_LIVE API tool (<https://nsidc.org/apps/itslive-search/docs>, last access: 1 March 2022). In the near future the data will also be accessible through NASA's Earthdata cloud and the National Snow and Ice Data Center. Other access options that facilitate time series analysis can be found by going to the project website (<https://its-live.jpl.nasa.gov>, last access: 1 March 2022).

The products are created using the input dataset as introduced above in Sect. 2.1.1 and the feature tracking processing chain detailed in Sect. 2.1.3. Each data granule consists of maps of land ice velocities over the spatial extent of the individual Sentinel-1 image pair at the specific epoch of data acquisition. The image-pair data product provides the most granular data for studying glacier change

Table 3. Sentinel-1 image pairs used for validation of the algorithms. All image pairs were acquired with the interferometric wide swath (IW) single look complex (SLC) mode. Only HH-pol is used. The pixel spacing is 3.67 m in ground range and 15.59 m in azimuth. The parenthesis of “(A/B)” denotes the Sentinel-1A image was acquired prior to the Sentinel-1B image, and vice versa.

Region 1 (path: 90/frame: 222, 227; ascending)	Region 2 (path: 31/frame: 253; ascending)	Region 3 (path: 112/frame: 350; descending)	Region 3 (path: 31/frame: 233, 238; ascending)
20170104–20170110 (A/B)	20171226–20180101 (A/B)	20161002–20161008 (A/B)	20171226–20180101 (A/B)
20170221–20170227 (A/B)	20161225–20161231 (B/A)	20161231–20170106 (B/A)	
20170404–20170410 (B/A)	20181227–20190102 (B/A)	20170331–20170406 (A/B)	
20170404–20170416 (B/B)		20170711–20170717 (B/A)	
20170404–20170422 (B/A)		20170927–20171003 (A/B)	
20170703–20170709 (A/B)		20171226–20180101 (B/A)	
20171001–20171007 (B/A)		20180326–20180401 (A/B)	
		20180630–20180706 (A/B)	
		20180928–20181004 (B/A)	
		20181227–20190102 (A/B)	

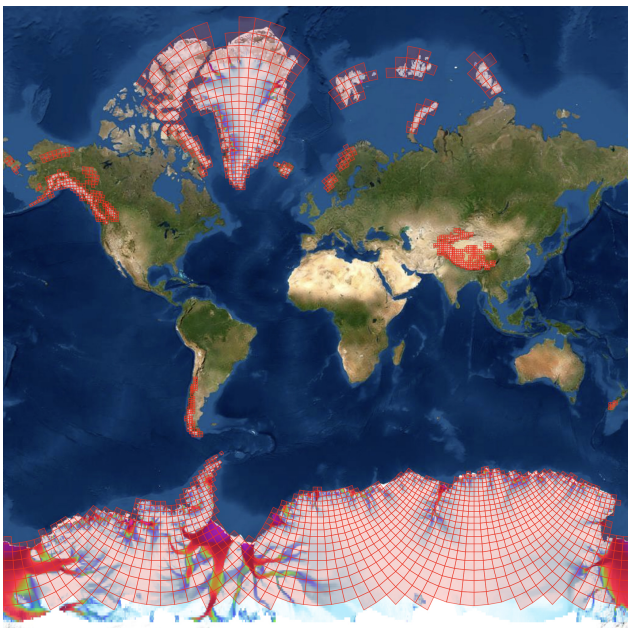


Figure 2. Global view of the spatial coverage of the ITS_LIVE Version 2 dataset (with Sentinel-1 available between 78° S and 81° N) which include image-pair products, as well as cloud optimized datacubes that contain all ITS_LIVE image-pair products. The ITS_LIVE Version 1.0 Landsat-derived ice velocity mosaic map is overlaid onto the global optical image as a reference velocity map, where the red boxes represent the spatial extents of the datacubes.

and is released as an independent data product to the end-users. This product serves as the basis for the upcoming ITS_LIVE Version 2 datacube and mosaic products. All of the Sentinel-1A (launched 3 April 2014) and Sentinel-1B (launched 25 April 2016) image pairs with a maximum time separation of 12 d, with a goal of extending to 60 d, are pro-

cessed into image-pair data products covering the globe (see Fig. 2) within the Sentinel-1 latitude limits (78° S–81° N) that include all large glacierized regions (roughly >25 km²), depending on data availability and quality. Here, the offset tracking at a given grid point is defined as “valid” if the determined pixel displacement using the current search chip passes the NDC filter based on the similarity with adjacent chips, as further discussed in Sect. 2.2. The spatial extent of the image pair encompasses the valid offsets for that pair. This means that two granules with the same Sentinel-1 orbit/frame designations may have different extents depending on offset tracking success: if the input images were largely contaminated by temporal decorrelation and/or atmospheric disturbance effects, then the extent of the output can be significantly reduced compared to the extent of the input image.

Image-pair products span the time period from the launch date of the corresponding sensors (e.g., Sentinel-1A–Sentinel-1A image pairs are available after the Sentinel-1A launch date, Sentinel-1B–Sentinel-1B and Sentinel-1A–Sentinel-1B or Sentinel-1B–Sentinel-1A image pairs are available after the launch date of Sentinel-1B) to present with a project goal of providing <3 months latency from the date of acquisition. The separation times for the image pairs vary from 6 d to 12 d for all sensor combinations, with the goal of extending to 60 d with multiples of 6 d separation dependent on funding. As a rule of thumb, for working with individual image-pair products over fast-flowing glacierized regions where rapid temporal decorrelation of radar signals is expected, using shorter separation times if available (e.g., 6 d; Sentinel-1A–Sentinel-1B or equivalently Sentinel-1B–Sentinel-1A) usually has better data quality than longer ones (e.g., 12 d or larger; Sentinel-1A–Sentinel-1A or Sentinel-1B–Sentinel-1B) due to less temporal decorrelation, which has been investigated by Friedl et al., 2021 and Solgaard et al., 2021. However, for observing slow-moving targets, all image-pair products with various separation times need to be

considered to fully capture both the short-term and long-term variability of the velocities, such as in studying the seasonal ice dynamics (Greene et al., 2020).

All output variables are provided on the same 120 m grid in the same map projection as the input dataset detailed in Sect. 2.1.1. The effective spatial resolution in offset tracking varies spatially with the progressive search chip size (Fig. 1d–e; from 240 m to 1920 m), where fast-flowing glaciers are characterized by smaller chip sizes (lower precision but finer resolution, e.g., 240 m), and the stable or slow-flowing ice uses larger chip sizes (lower resolution but higher precision, e.g., 1920 m). The output data (Table 2) are packaged in a single NetCDF, using Climate Forecast (CF) Version 1.8 conventions. Individual NetCDF files are between 5 and 15 MB in size. The x and y velocities (v_x and v_y), velocity magnitude (v) and its error (v_error), and $chip_size_height$, $chip_size_width$, $interp_mask$, and img_pair_info are standard output variables for all ITS_LIVE image-pair velocity products (i.e., both optical and radar). The remaining variables listed in Table 2 are specific to radar data, such as the slant range (LOS) and azimuth (along-track) velocities (v_r and v_a , respectively) that are provided in native radar viewing geometry. The LOS parameters (M11 and M12) are provided in the output for each image pair to facilitate the inversion for x/y horizontal velocity when using two independent slant range measurements (i.e., one ascending image pair and one descending image pair). This is useful to correct for ionosphere disturbance effects on the azimuth offset (Sect. 3.2).

When velocities are calculated from imagery that has been map projected (i.e., optical imagery), this can introduce scale errors of up to a few percent that are dependent on the projection used and the location of the imagery. Unlike ITS_LIVE Version 1 products, ITS_LIVE Version 2 products (both radar and optical) have not been corrected for the scale distortion due to calculating velocities from map-projected imagery (i.e., velocities are relative to map coordinates). For Sentinel-1 image pairs, velocities referenced to map coordinates (i.e., v_x , v_y , and v) are provided in map projected distance. The implications of this are detailed further in the Version 2 documentation (<http://its-live.jpl.nasa.gov/>, last access: 1 March 2022).

2.1.3 Processing chain

The Sentinel-1 single look complex (SLC) image pairs are preprocessed using the ISCE software prior to dense offset tracking, where the two SLC images are precisely coregistered using the satellite orbit geometry. Dense offset tracking relies heavily on two Python modules: *Geogrid* and *autoRIFT*, followed by a NetCDF packaging program (all of which are open access and available at <https://github.com/nasa-jpl/autoRIFT>, last access: 1 March 2022). As described by Lei et al. (2021a), the Sentinel-1 orbit information is used by *Geogrid* to transform all of the input parameters listed

in Table 2 from map-projected Cartesian coordinates (northing/easting) into radar range/azimuth coordinates (pixel index and displacement). The inputs are translated to radar coordinates but not resampled (i.e., remains in the original 120 m grid). Inputs are cropped to the spatial extent of the image-pair overlap. At this stage, all distances (in m) and velocities (in m yr^{-1}) have been converted to pixel distances in range/azimuth, where velocities are multiplied by the time separation between images to convert from a rate to a distance. The approach of defining a regular output grid in map-projected coordinates and then converting to an irregular grid in radar coordinates is somewhat unique, yet powerful. The approach avoids the need for any reprojection of the imagery or resampling of the derived velocity fields when moving between radar and map coordinates. This eliminates costly interpolation, and resulting artifacts, in the final product.

Once inputs (Table 2) have been mapped/converted to radar coordinates/units they are passed to the *autoRIFT* module which performs the dense range and azimuth offset search between the two images. As illustrated in Fig. 3, *autoRIFT* finds the displacement between two images using a nested grid design, sparse/dense combinative searching strategy, and disparity filtering technique that result in significant performance gains and that are detailed in Gardner et al. (2018) and Lei et al. (2021a). *autoRIFT* then cycles from the minimum to the maximum chip size (Fig. 1d–e) at multiples of 2 until a valid offset match is found, returning the value of the first valid offset (finest resolution). Each progressive chip size is a factor of 2 larger than the previous and is solved on a map-projected coordinate grid that satisfies a 50 % overlap between adjacent search chips of the same size (i.e., a $240 \text{ m} \times 240 \text{ m}$ chip is solved on a constant 120 m grid, a $480 \text{ m} \times 480 \text{ m}$ chip is solved on a constant 240 m grid). This change in sample rate is termed a “nested grid” design. *autoRIFT* employs the NDC filter to distinguish valid offset matches from random noise. Earlier versions of *autoRIFT* did not permit overlap between adjacent search chips. To accommodate overlapping chips, adjustments were made to the NDC filter parameters and are detailed in Sect. 2.2. For each chip size used, a sparse search (1/8 sample rate) is performed to identify and exclude areas that do not pass the NDC filter. A dense search is then performed for all valid areas at the full sample rate, with search center and range informed by the results of the sparse search. This sparse/dense combinative searching strategy substantially improves computational efficiency (i.e., 2 orders of magnitude improvement; as further discussed in Sect. 2.4). *autoRIFT* further improves efficiency without sacrificing accuracy or resolution by employing OpenCV’s C++ functions for normalized cross-correlation (NCC), a downstream search routine to reduce the search range, subpixel offset estimation using a Gaussian pyramid upsampling algorithm and various high-pass filtering options to preprocess the image pair with data compression (Gardner et al., 2018; Lei et al., 2021a). In Sect. 2.3 we

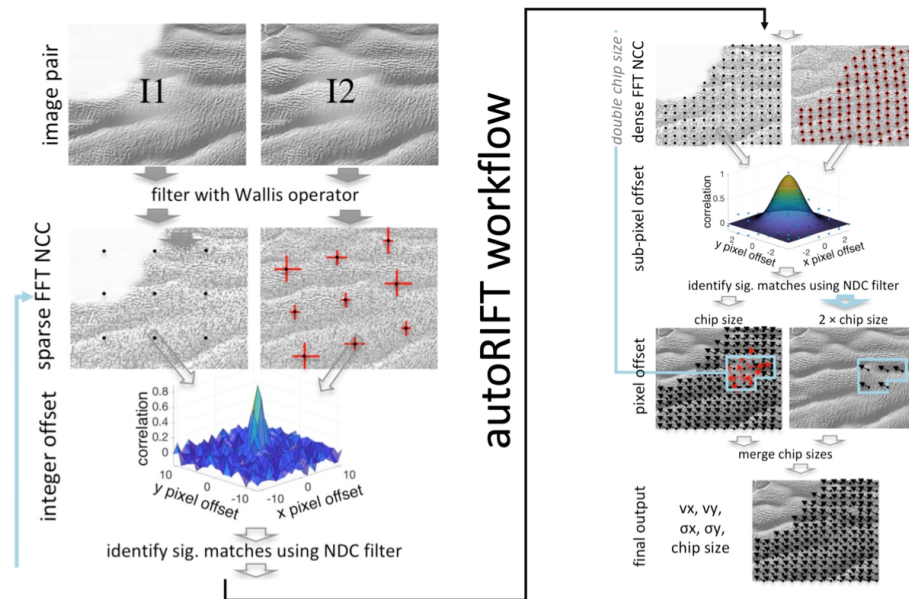


Figure 3. Composite diagram showing the *autoRIFT* workflow.

describe the addition of chip size-dependent subpixel oversampling ratios that further enhance performance.

Sentinel-1 range and azimuth offset estimates are then calibrated for the subswath and full swath-dependent geolocation biases that are identified for Sentinel-1A/B combinations and are affected by an intersatellite systematic bias (Sect. 3.1). Offsets are then converted back to map-projected coordinates/units using *Geogrid*. All of the output data (Table 2) are packed as a NetCDF with accompanying metadata.

2.2 Fine output grid with improved NDC filter

A key component of *autoRIFT* that identifies and removes poor feature matches is the implementation of the NDC filter. In this section, we document updates to the NDC filter for handling finer grid spacings with overlapping search chips. As illustrated in Fig. 4a, the original NDC filter assumed chip independence (i.e., no overlap between adjacent chips). However, when oversampling is desired, adjacent chips overlap (e.g., Fig. 4b shows the case of 50% overlap). This results in information being shared between neighboring search chips, changing the signal-to-noise statistics. For this reason, we modified the NDC filter parameters to account for the change in the signal-to-noise statistics.

As first developed in Gardner et al. (2018) and also described in Lei et al. (2021a), the NDC filter in *autoRIFT* identifies and removes low-coherence displacement results based on displacement disparity thresholds that are normalized to the local search distance. This is done to normalize changes in the amplitude of the noise that scales linearly with the search distance. The NDC filter is defined with a few filter parameters: *FracValid* (fraction of valid grid points within

the filter window size; default is $8/25$, e.g., 8 valid points for a 5×5 filter window), *FracSearch* (fraction of displacement disparity normalized to search distance; default is 0.2), *FiltWidth* (filter window size; default is 5), *Iter* (number of iterations that the filter is applied; default is 3) and *MadScalar* (multiplicative factor for thresholding the displacement disparity; default is 4). The NDC filter is applied as a sliding window filter. Here we provide an example of the NDC filter applied using a 5×5 filter window size:

- Normalize the displacement estimates by the search distance.
- Compute the normalized displacement disparity in reference to the central grid point for all the grid points within the filter window and count the number of grid points that have displacement disparity smaller than *FracSearch* (threshold of maximum disparity with the default value of 0.2).
- If the number of grid points in the above step is greater than or equal to $FracValid \times FiltWidth^2$ (by definition, it is the threshold of valid points within the filter window, e.g., $8/25 \times 5^2 = 8$ in this case), the central grid point is retained, otherwise it is discarded.
- A second condition check is then performed: the central grid point is retained if the deviation of its displacement from the median value of this filter window is less than the median absolute deviation (MAD) multiplied by *MadScalar*. This step is repeated for *Iter* times for the entire displacement field by discarding poor offset matches in each iteration.

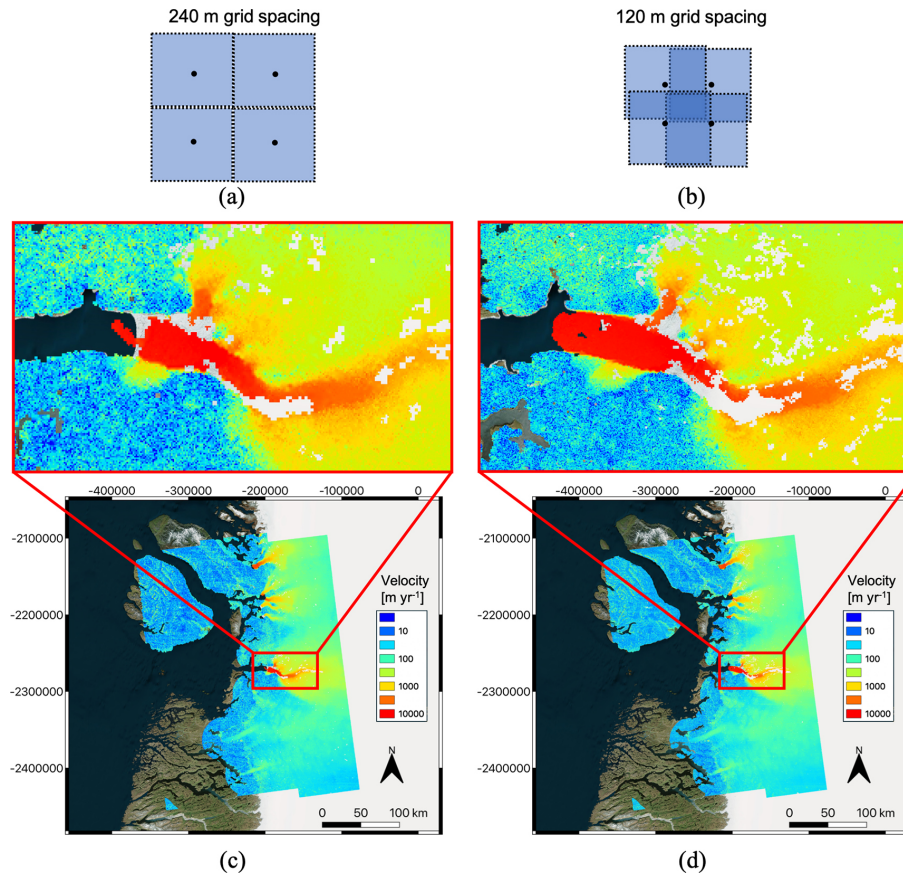


Figure 4. Comparison between a 240 m posting grid and a 120 m posting grid: (a) 240 m grid with non-overlapping search chips, (b) 120 m grid with 50 % overlapping search chips, (c) *autoRIFT*-estimated ice velocity magnitude for 240 m grid, (d) *autoRIFT*-estimated ice velocity magnitude for 120 m grid. The same minimum chip size of 240 m is used for both cases. For (c) and (d), the Sentinel-1 image pair 20170404–20170410 is used in Region 1 (with the close up at the Jakobshavn Isbræ Glacier). Background: © Microsoft Bing Maps 2022.

e. If all the above conditional checks are passed, the central grid point is retained, otherwise it is discarded.

The filter parameters need to be adjusted when there is overlap between adjacent chips to maintain the same filter performance as in the non-overlap scenario. For the 50 % overlap case illustrated in Fig. 4b, the default *FracSearch* value of 0.2 can be used but *FracValid* needs to be made larger due to the interdependence of neighboring offsets. As an extreme case, with 0 % overlap, *FracValid* should be the same as the default value for the non-overlap case and with 100 % overlap, *FracValid* should be 1. Therefore, considering these extreme cases and through trial and error, we found that the following formula works well for all cases considered:

$$FracValid_{w_overlap} = FracValid_{wo_overlap} \times (1 - overlap) + overlap^2, \quad (1)$$

where *FracValid_{w_overlap}* and *FracValid_{wo_overlap}* are the *FracValid* parameters with and without overlap, respectively and "overlap" is the percentage of the overlap (e.g., 50 %

in Fig. 4b). As the adjacent grid points share information, the filter window size needs to be enlarged by a factor of 1/overlap in order to have an equivalent number of independent samples within a filter window

$$FiltWidth_{w_overlap} = \text{round} \left[\frac{(FiltWidth_{wo_overlap} - 1)}{overlap + 1} \right], \quad (2)$$

where *FiltWidth_{w_overlap}* and *FiltWidth_{wo_overlap}* are the *FiltWidth* parameters with and without overlap, respectively and $\text{round}[\cdot]$ is the round to integer operation. Using Eqs. (1) and (2), the NDC filter performance for the overlapping chips is comparable to the non-overlap scenario. Figure 4c demonstrates the ice velocity magnitude from the Sentinel-1 image pair 20170404–20170410 centered over the Jakobshavn Isbræ Glacier in Region 1 (Fig. 1a) using the earlier 240 m posting grid with non-overlapping search chip of size 240 m (Fig. 4a). Figure 4d shows the results for the 120 m posting grid using a search chip of size 240 m with 50 % overlap between adjacent search chips (Fig. 4b). From the results in Fig. 4c, d, it can be seen that the region of interest (ROI) representing valid pixels between the two cases is very similar,

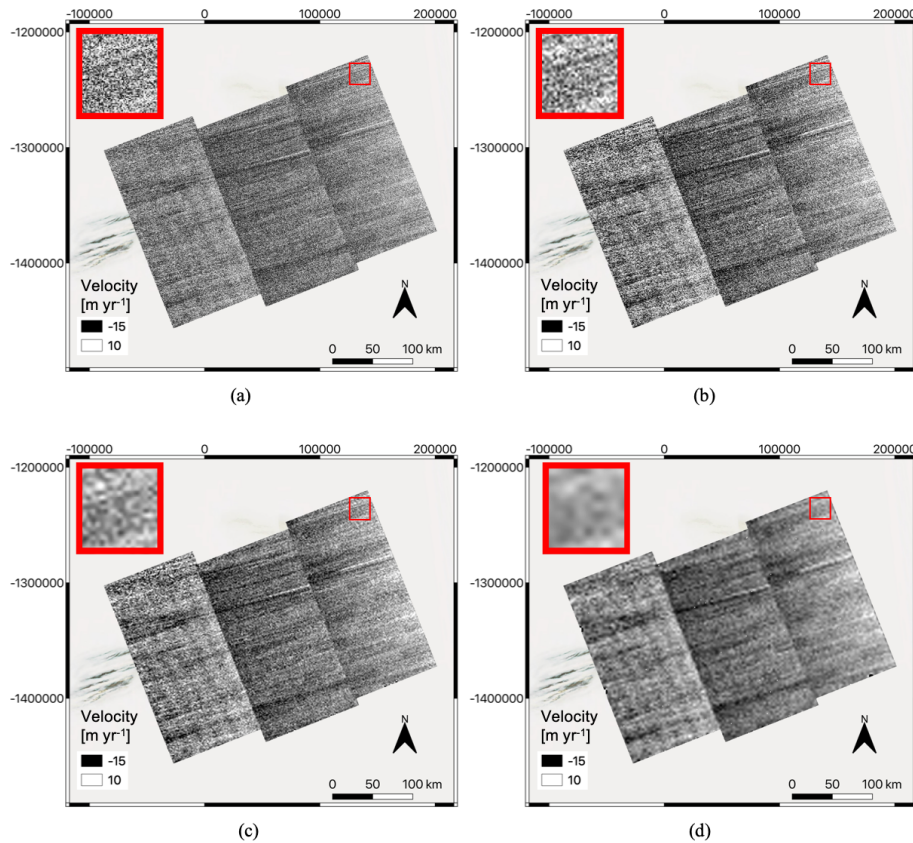


Figure 5. X-velocity from offset tracking using chip sizes of (a) 240 m, (b) 480 m, (c) 960 m, and (d) 1920 m. The same subpixel oversampling ratio of 1/128 is used for all cases. The Region 2 Sentinel-1 image pair 20171226–20180101 is used. Background: © Microsoft Bing Maps 2022.

implying the comparable filter performance, while the 120 m grid indeed provides higher resolution estimates without sacrificing signal-to-noise over the ROI.

2.3 Search chip size-dependent subpixel oversampling ratio

autoRIFT identifies the integer offset between two images as the maximum NCC value for all possible locations of the search chip (subset of image 2) within the search window (subset of image 1). To identify the subpixel component of the offset, an oversampled surface is fitted to the pixel NCC values to create a smooth surface from which the subpixel offset can be estimated. Careful consideration must be taken on how the surface is fitted, as some approaches can lead to biases in offset estimates (Stein et al., 2006). To minimize such bias, *autoRIFT* employs a Gaussian pyramid upsampling algorithm. Surface fitting is computationally expensive, increasing substantially with the oversampling ratio. Therefore, subpixel peak finding should consider the inherently achievable precision of the underlying data in determining the optimal oversampling ratio. An oversampling ratio that is too coarse will result in less precise data, while an oversam-

pling ratio that is too fine will result in unnecessary computational overload. In addition, there is an inherent relationship between the size of the search chip and the maximum achievable precision: larger chip size results in higher achievable precision and vice versa. Therefore, it is desirable to select an optimal trade-off between efficiency and the precision of the subpixel oversampling ratio as a function of chip size, as in Lei et al. (2021a).

We consider 4 chip sizes: 240, 480, 960 and 1920 m, and 4 subpixel oversampling ratios: 1/16, 1/32, 1/64 and 1/128. To investigate the relation between chip size-dependent accuracy and oversampling ratio we select the Sentinel-1 image pair 20171226–20180101 in Region 2. Region 2 represents a slow-moving ice surface with no detectable gradient in flow and all four chip sizes result in valid offset tracking results. Results determined using an oversampling ratio of 1/128 are considered most precise. Figure 5 shows the x -velocity (v_x) for various chip sizes using an oversampling ratio of 1/128. Note that the subswath bias (visible at subswath boundaries) with azimuth streaks that are noticeable in Fig. 5 are due to the Sentinel-1 systematic geolocation bias and ionosphere delay effects, both of which are discussed and accounted for using the methods presented in Sect. 3. From Fig. 5 it can

be seen that smaller chip sizes (240 and 480 m) have a high standard deviation (noise), while larger chip sizes (960 and 1920 m) have lower standard deviation (more precise) in the displacement estimates. The question we now try to answer is: is the computational cost of a finer oversampling ratio justified by an improvement in precision? To determine this balance, we examine changes in the standard deviation as a function of the oversampling ratio for each chip size. A summary of the results is provided in Table 4.

From our analysis we find that a coarser oversampling ratio of 1/32 (1/64), for a chip size of 240 m (480 m), results in a modest increase in noise (<3 %) with up to a factor of 3 improvement in performance (Table 4). We therefore select these oversampling ratios for the smaller chip sizes. For chip sizes of 960 and 1920 m we see a substantial (30 % for 960 m and 80 % for 1920 m) increase in noise with a decrease in oversample ratio (1/64). Therefore, we select an oversample ratio of 1/128 for these larger chip sizes. This intelligent oversampling ratio is adopted in *autoRIFT* for generating the ITS_LIVE Sentinel-1 offset tracking products. The optimal oversampling ratio is dependent on the information content of the input imagery and would require a similar analysis, as conducted here, for application to other satellite missions. For Landsat-8 data *autoRIFT* uses an oversampling ratio of 1/16, 1/32, 1/64 and 1/64 for chip sizes of 240, 480, 960 and 1920 m, respectively. A coarser oversampling ratio leads to coarser velocity discretization. This can be seen when plotting chip size-dependent histograms of v_a and v_r in which values are clustered according to the oversampling ratio. A smoother histogram can be achieved with a finer oversampling ratio but, due to the limitations of the data, a finer oversampling ratio will not achieve higher accuracy. The precision and accuracy can be increased through postprocessing of the data (e.g., spatial or temporal smoothing).

2.4 *autoRIFT* runtime analysis

As previously shown by Lei et al. (2021a), *autoRIFT* outperforms the widely used “dense ampcore” feature tracking algorithm (CPU version) that is the default feature tracker included in the NASA/JPL ISCE software, with 2 orders of magnitude improvement in efficiency and >20 % improvement in accuracy. Here we expand the apples to apples comparison between *autoRIFT* and ampcore that was conducted by Lei et al. (2021a). We use seven Region-1 Sentinel-1 image pairs with the same *autoRIFT* and ampcore setting as used by Lei et al. (2021a: Table 4). The runtime and accuracy improvements of *autoRIFT* compared to ampcore are illustrated in Fig. 6 as a function of the % valid ROI (i.e., the % of valid pixels returned by *autoRIFT*). In Fig. 6a, an exponential function was fitted to the runtime data points with respect to ROI. The figure shows that *autoRIFT* is about 150 times faster than ampcore for Sentinel-1 image pairs with high correlation between images (large ROI) and up to 208 times faster when there is low correlation between images (low

ROI). This increase in runtime improvement with a decrease in ROI is due to *autoRIFT*'s sparse search that excludes areas of low correlation before executing a dense search. Regarding the accuracy of both feature trackers, we refer to the standard deviation of x/y pixel displacements over stable surfaces (Fig. 1f). Here, x/y represents the dimensions in the native radar image coordinates, i.e., range/azimuth. Since dense ampcore does not employ any filtering to remove bad matches, we calculated the error of dense ampcore results wherever *autoRIFT* produced reliable estimates. As shown in Fig. 6b, *autoRIFT* provides an improvement in accuracy on the order of 20–50 % (33 % when averaged across all 7 image pairs). Some of the improvement can be attributed to *autoRIFT*'s ability to narrow the search range of the dense search based on information gained from the sparse search (a form of regularization). Different approaches to locating the subpixel displacement may also contribute to *autoRIFT*'s improved accuracy (e.g., Gaussian pyramid upsampling algorithm).

3 ITS_LIVE Sentinel-1 image-pair product calibration and error correction

In this section we demonstrate approaches to calibrate and correct for errors in the ITS_LIVE Sentinel-1 image-pair product. Section 3.1 discusses the systematic geolocation bias calibration (both subswath and full swath-dependent). In Sect. 3.2, we introduce a method of correcting for the ionosphere disturbance effects that contaminate radar azimuth measurements, which uses the radar LOS measurements from two image pairs with differing acquisition geometries (i.e., ascending and descending).

3.1 Geolocation bias calibration

As pointed out in Gisinger et al. (2020), Sentinel-1's azimuth Doppler frequency modulation (FM) rate can be offset compared with the modeled value for each of the three subswaths in the TOPS acquisition mode because of the use of constant terrain height for FM rate computation for extended areas of observed terrain (spatial extent of the SAR image). In reality, each of the three subswaths has its own azimuth FM rate. This systematic mismatch can cause both full-swath and subswath-dependent pixel shift (geolocation bias) along the radar azimuth direction when focusing radar signals. Full-swath and subswath-dependent systematic geolocation errors along the radar range direction also result from the bistatic nature of the antenna, i.e., transmitting and receiving are not simultaneous, which is neglected in the current SLC processing and thus introduces a residual Doppler shift error when focusing the radar pulses in the range direction (Gisinger et al., 2020). Several studies (Gisinger et al., 2020; Solgaard et al., 2021; Schubert et al., 2017) have investigated the full-swath-dependent range/azimuth geolocation bias of Sentinel-1 IW products, and also mentioned the ex-

Table 4. Selection of subpixel oversampling ratios for various chip sizes. The first four rows show the results for the highest oversampling ratio (1/128), which is used to characterize the maximum achievable precision. The last four rows show the results for the lowest oversampling ratio that provides negligible degradation (1–3 %) in precision. The column of “nearest oversampling ratio” is selected to match the maximum achievable precision and thus determine the optimal oversampling ratios to be used for each chip size (first column of the last four rows).

Oversampling ratio	Chip size [m]	Runtime [s]	x/y precision [pixel]	Nearest oversampling ratio
1/128	1920	52.9	0.0086/0.0097	1/128 \approx 0.0078
1/128	960	83.5	0.0118/0.0122	1/128 \approx 0.0078 or 1/64 \approx 0.0156
1/128	480	200.8	0.0155/0.0185	1/64 \approx 0.0156
1/128	240	661.5	0.0321/0.0392	1/32 = 0.0312
1/128	1920	52.9	0.0086/0.0097	–
1/128	960	83.5	0.0118/0.0122	–
1/64	480	110.4	0.0158/0.0188	–
1/32	240	188.1	0.0332/0.0401	–

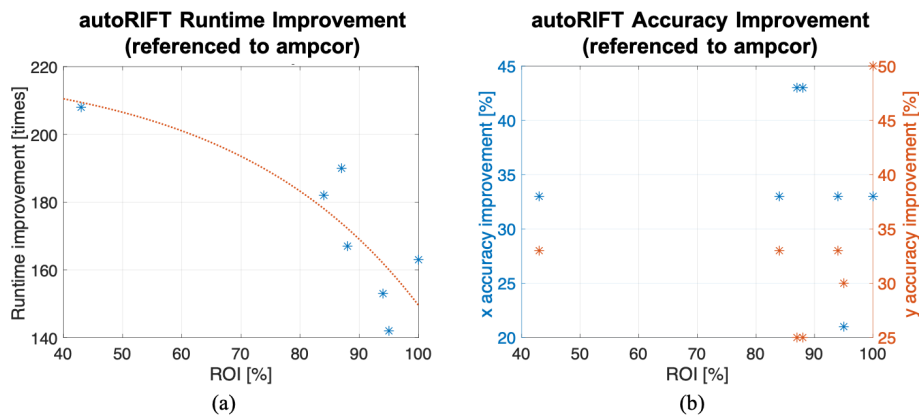


Figure 6. Apples to apples comparison between *autoRIFT* and *ampcor*: (a) runtime improvement, (b) x/y (range/azimuth) accuracy improvement. Both *autoRIFT* and *ampcor* use the same setting for offset tracking as in Lei et al. (2021a): chip size of 64×64 , grid spacing of 64×64 , and search limit of 62×16 . The 7 Sentinel-1 image pairs in Region 1 (frame 222 only) are used.

istence of the subswath-dependent geolocation bias. At the time of writing, besides the subswath-dependent range bias estimates (Zhang et al., 2022), we are not aware of any existing subswath-dependent geolocation bias (both range and azimuth) correction. In the following subsections we demonstrate the calibration of both types of geolocation bias for the ITS_LIVE Sentinel-1 ice velocity products.

3.1.1 Subswath-dependent geolocation bias

When working with Sentinel-1 image pairs, systematic geolocation biases cancel out in the resulting offset maps when using data from the same sensor (both from Sentinel-1A or both from Sentinel-1B); however, this is not the case when using a combination of the two (one from Sentinel-1A and the other from Sentinel-1B). For this reason, we focus on corrections that need to be applied when image pairs are composed of images from differing sensors.

As mentioned in Sect. 2.3 (Fig. 5), there is subswath-dependent velocity bias between the three subswaths. We illustrate this effect by showing both the raw slant range and azimuth velocity products (v_r and v_a from Table 2) in Fig. 7a, b for the Sentinel-1 pair 20171226–20180101 in Region 2, where the range-dependent variation of the velocity (by averaging each range line/bin) is found in Fig. 7c. Figure 7c clearly demonstrates the subswath mismatch. To correct for the subswath mismatch, we select two areas in the interior of Greenland (Regions 2 and 3) with 14 Sentinel-1A/B image pairs (in Table 3) that contain small and smooth gradients in ice motion and ionospheric effects, and are thus more suitable for calibration of biases. Only 11 out of the 14 pairs are eventually shown in Fig. 8 after eliminating 3 noisy pairs contaminated by strong ionosphere scintillation (Jiao et al., 2013). We calculate the inter-subswath bias by taking the difference of the median values on either side of the subswath boundaries of the slant range and azimuth offsets. The results of this analysis are shown in Fig. 8.

From Fig. 8, the average offset biases between subswaths 2 and 1 are -0.010 pixels (slant-range) and 0.019 pixels (azimuth), while the estimates for subswaths 3 and 2 are -0.007 pixels (slant range) and 0.006 pixels (azimuth), which uses the pair convention of Sentinel-1A being acquired prior to Sentinel-1B. These inter-subswath bias estimates are similar to the numbers reported in the other studies over various regions of the globe, e.g., -0.0082 pixels (slant range) between subswath 2 and 1, and -0.0073 pixels (slant range) between subswaths 3 and 2 (Zhang et al., 2022). Therefore, the inter-subswath bias estimates are considered systematic biases and used in generating our ITS_LIVE Sentinel-1 image-pair products for calibrating the subswath-dependent geolocation bias. The performance of the correction is illustrated in Fig. 7d–f, where both the velocity maps and the range-dependent variation curve show greatly improved matching between subswaths (i.e., there is little or no step change in velocity when transitioning between subswath boundaries).

3.1.2 Full-swath-dependent geolocation bias

After the subswath-dependent geolocation error correction is applied, we apply additional corrections to remove full-swath-dependent biases. As reported in previous studies (Gisinger et al., 2020; Solgaard et al., 2021; Schubert et al., 2017), the geolocation error for the full-swath can be measured by comparing the SLC image pixel geolocations or resulting offset tracking velocity to ground control points, e.g., array of corner reflectors or stable terrain. Locally determined estimates can then be applied to all the Sentinel-1 image pairs as a static calibration assuming that the error is systematic in nature. Conceptually, this calibration is similar to referencing an interferogram to a known reference point (e.g., GPS station) in InSAR analysis. In this paper, we adopt a similar approach but apply a unique correction to each Sentinel-1 image pair by separately calibrating to any overlapping stable surfaces, as has been done in our previous work (Gardner et al., 2018; Lei et al., 2021a). We determine the calibration surface using a “stable surface” mask (Fig. 1f) that is defined as any area consisting of ice-free terrain and/or slow-moving ice defined using an a priori reference velocity ($<15 \text{ m yr}^{-1}$; Fig. 1f). When image-pair offsets do not intersect any valid “stable surface” we calibrate the slowest 25 % velocity magnitude, as defined by an a priori velocity field, to an a priori reference velocity. We examine the performance of these two approaches for full-swath-dependent geolocation bias calibration using all 20 Sentinel-1A/B image pairs (Table 3) in Regions 1, 2 and 3. Results are illustrated in Fig. 9.

The mean “stable surface” mask calibrated velocity bias is -4.1 in slant range and -26.8 m yr^{-1} in azimuth using the pair convention of Sentinel-1A being acquired prior to Sentinel-1B with a 6 d time separation. Note that in this paper, we report the velocity calibration bias (rather than pixel offset bias in Sect. 3.1.1 or offset bias in meters) for the full-

swath-dependent geolocation bias, in order to better compare with the values reported in the literature as shown below. One can convert from one to another by using the 6 d time separation and/or slant range/azimuth pixel size. Using the slowest 25 % velocities, the mean velocity bias is estimated to be -4.0 in slant range and -27.1 m yr^{-1} in azimuth. Hence, by using a stable surface mask (which is available in most regions) or the slowest 25 % velocities, our dynamically calibrated estimates of geolocation bias are comparable to those reported in previous work over various regions of the globe and thus confirmed to be systematic biases, e.g., -8.8 in slant range and -28.8 m yr^{-1} in azimuth (Solgaard et al., 2021), -9.7 in slant range and -24.4 m yr^{-1} in azimuth for the extended timing annotation dataset (ETAD) correction (Gisinger et al., 2020) as well as -5.3 , -6.4 , -7.5 m yr^{-1} in slant range for each of the three subswaths (Zhang et al., 2022). Therefore, these bias estimates are used in generating our ITS_LIVE Sentinel-1 image-pair products for calibrating the full-swath-dependent geolocation bias.

The small difference between our estimates and those reported in the literature can be due to the fact that we first applied the subswath-dependent geolocation bias correction. We note that the method of using the slowest 25 % provides good estimates of the velocity bias, almost equivalent to those by using an external stable surface mask. In the processing, we only calibrate to the slowest 25 % when there is insufficient overlap with the “stable surface” mask. Note the above velocity bias estimates are specifically referenced to 6 d Sentinel-1A/B image pairs with Sentinel-1A acquired prior to Sentinel-1B.

Scalar full-swath-dependent bias corrections are applied and stored as `stable_shift_mask` and `stable_shift_slow` for each of the velocity variable (e.g., v_x , v_y , v_r and v_a) in our ITS_LIVE Sentinel-1 product (Table 2). After the geolocation corrections are applied, the uncertainties in the velocities are calculated (Lei et al., 2021a) over the intersecting “stable surfaces” area when there is sufficient overlap, otherwise the calculations are made for the slowest 25 %. Uncertainties are taken as the standard error between the calculated and the reference velocities, as described in Gardner et al. (2018) and elaborated in Lei et al. (2021a). Hence, these estimated uncertainties are assigned as scalar attributes (named “error”) to each of the 2-D velocity fields (v_x , v_y , v_r and v_a). However, the uncertainty of the velocity magnitude (v), namely v_error , must be estimated using the following error propagation formula:

$$v_error = \sqrt{\left(\frac{v_x}{v} \cdot vx_error\right)^2 + \left(\frac{v_y}{v} \cdot vy_error\right)^2}, \quad (3)$$

where “ vx_error ” and “ vy_error ” are scalar uncertainties of each 2-D velocity field (v_x and v_y , respectively) estimated over stable (or slowest 25 %) surfaces, and all of v_x , v_y and v are 2-D velocity fields, implying that the velocity magnitude uncertainty v_error is a 2-D field as well. In Sect. 4, we will show the uncertainty estimates for the 2-D velocity field of

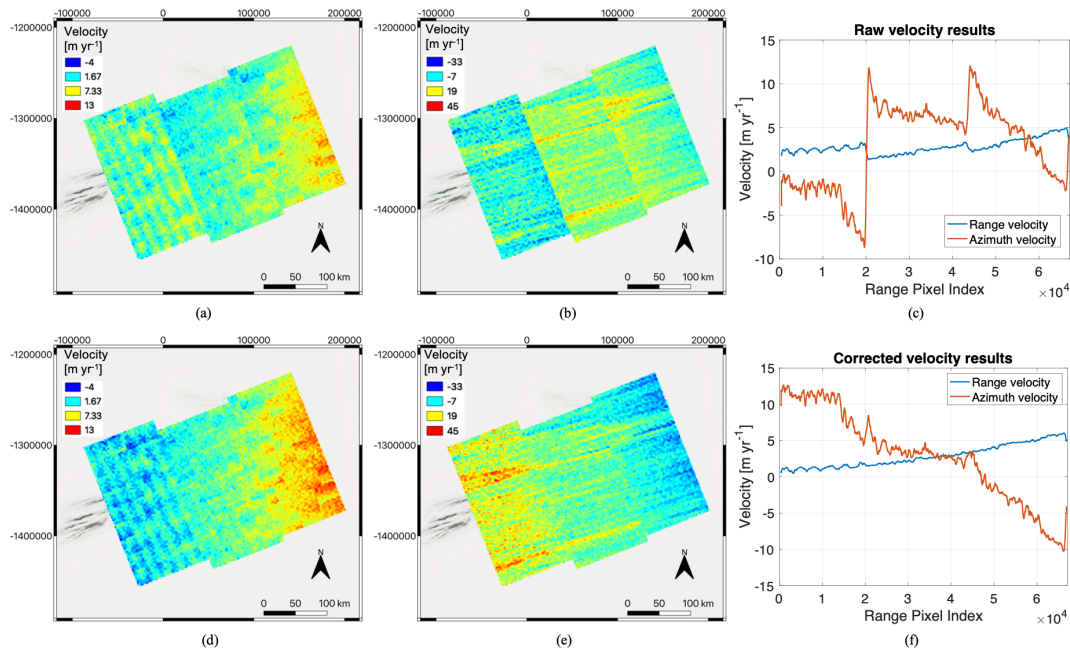


Figure 7. Illustration of subswath-dependent geolocation bias and calibration: (a) raw slant range velocity, (b) raw azimuth velocity, (c) range-dependent variation of raw velocity (averaged for each range line/bin), (d) corrected slant range velocity, (e) corrected azimuth velocity, (f) range-dependent variation of corrected velocity (averaged for each range line/bin). The Sentinel-1 image pair 20171226–20180101 in Region 2 is used here. Background: © Microsoft Bing Maps 2022.

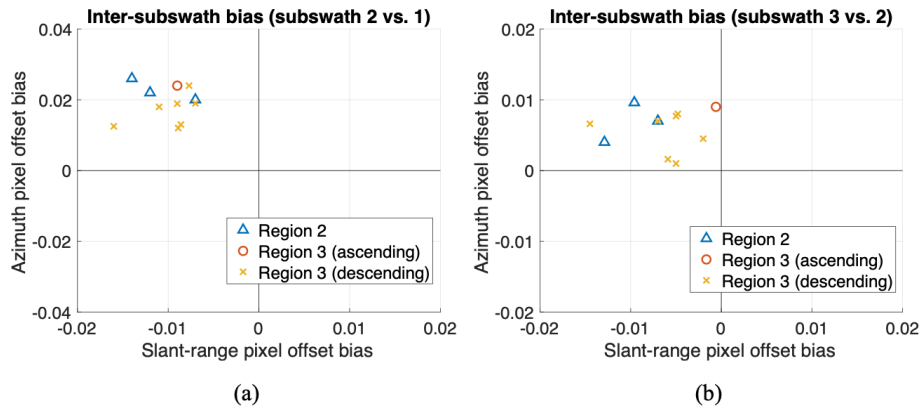


Figure 8. Inter-subswath bias of slant range and azimuth offsets: (a) subswath 2 versus 1, (b) subswath 3 versus 2. The 11 Sentinel-1A/B image pairs in Region 2 and Region 3 are shown here.

v_x and v_y , along with the uncertainty of the velocity magnitude (v) calculated using Eq. (3), at different test sites of the globe using a large number of ITS_LIVE Version 2 Sentinel-1 image-pair products.

3.2 Ionosphere correction: ascending and descending combined velocity

Remaining velocity errors are dominated by atmosphere delay effects, particularly in the polar regions (Nagler et al., 2015; Solgaard et al., 2021). A common ionosphere effect on the offset tracking velocity products is azimuth pixel

shifts due to the linear along-track variation of the ionosphere phase delay within the synthetic aperture in SAR processing. The shift is proportional to the linear rate of the ionosphere phase delay and inversely to the azimuth FM rate of the SAR platform (Meyer et al., 2006; Liang et al., 2019). This azimuth pixel shift usually results in long stripe-like artifacts, also called “azimuth streaks”, in SAR-derived offset tracking maps. Such errors have been widely reported in the literature (Joughin et al., 1998; Gray et al., 2000; Joughin, 2002; Strozzi et al., 2008; Joughin et al., 2010; Mouginot et al., 2012; Rignot and Mouginot, 2012; Sánchez-Gómez

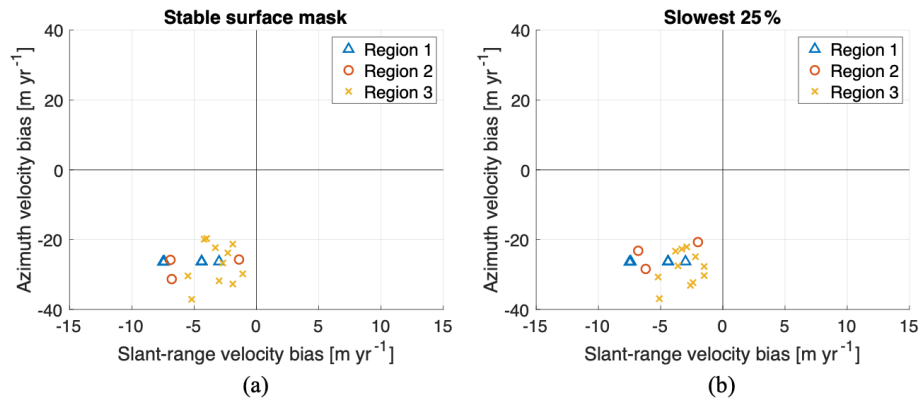


Figure 9. Full-swath geolocation bias-induced slant range and azimuth velocity bias: **(a)** with stable surface mask, **(b)** considering the slowest 25 % as stable surfaces. The 20 Sentinel-1A/B image pairs in Regions 1, 2 and 3 are used. We use the pair convention of Sentinel-1A acquired prior to Sentinel-1B with 6 d time separation.

and Navarro, 2017; Joughin et al., 2017; Liao et al., 2018). Traditional methods for removing these azimuth streaks are stacking or weighted averaging of multiple velocity time-series estimates (Rignot and Mouginot, 2012; Joughin et al., 2017), and combining InSAR LOS phase measurements from ascending and descending passes (Joughin et al., 1998; Sánchez-Gómez and Navarro, 2017).

Note that the uncertainty of offset tracking velocity is roughly 5 times worse for azimuth velocities than for the range ones when using TOPS mode Sentinel-1 image pairs, because the azimuth resolution is roughly 5 times coarser than in range. However, as mentioned above, the impact of ionosphere phase delay on offset tracking velocity that is more severe for azimuth velocities is irrespective of the resolution and due to the linear along-track variation of the ionosphere phase delay within the synthetic aperture of the SAR processing. Here we examine an approach to remove azimuth streaks in the ITS_LIVE Sentinel-1 image-pair products. This approach exploits the LOS (slant range) measurements from the SAR acquisitions, which has minimal impact from ionosphere disturbance.

With the LOS measurement from a single Sentinel-1 image pair (i.e., 1-D observation of displacement), the 2-D flow field is indeterminate. In the case of two image pairs with differing acquisition geometries (i.e., ascending and descending), we are provided with two independent LOS measurements from which the 2-D flow field can be determined. This approach has been applied to InSAR LOS phase as well as range offset measurements (Joughin et al., 1998, 2018; Sánchez-Gómez and Navarro, 2017). Here we demonstrate how to apply this correction approach to the offset tracking velocity layers in our ITS_LIVE Sentinel-1 image-pair products.

As described in Sect. 2.1.3 and in Lei et al. (2021a), the *Geogrid* module provides a look-up table of 2×2 conversion matrix between range/azimuth pixel displacements and x/y direction velocity fields. Here, the slope parallel assump-

tion (Joughin et al., 1998) is adopted, where surface displacement is assumed to be parallel to the local surface. Therefore, the z -direction (vertical) velocity can be further expressed as a function of the x/y direction velocities. Note this assumption becomes problematic over regions of known non-trivial vertical flow, e.g., slope and/or elevation changes.

Below we define the two elements from the first row of the conversion matrix as M11 and M12 (see Table 2; denoted as M_{11} and M_{12}). The conversion matrix elements M11 and M12 are stored in the final NetCDF file of the ITS_LIVE Sentinel-1 image-pair product with a 32 bit floating point to 16 bit integer data compression. The LOS (slant range) measurement of pixel displacement (denoted by D_r) can be related to the x/y direction velocity (v_x and v_y ; denoted by v_x and v_y) via the following relationship:

$$D_r^a = M_{11}^a v_x + M_{12}^a v_y, \tag{4}$$

for the ascending pair (with the superscript “a”) and

$$D_r^d = M_{11}^d v_x + M_{12}^d v_y, \tag{5}$$

for the descending pair (with the superscript “d”). Note that Eqs. (4) and (5) formulate a system of two linear equations with two unknowns. By inverting these two equations, we can solve for the velocity fields in map coordinates:

$$\begin{pmatrix} v_x \\ v_y \end{pmatrix} = \frac{1}{(M_{11}^a M_{12}^d - M_{12}^a M_{11}^d)} \begin{bmatrix} M_{12}^d & -M_{12}^a \\ -M_{11}^d & M_{11}^a \end{bmatrix} \begin{pmatrix} D_r^a \\ D_r^d \end{pmatrix}. \tag{6}$$

Thus, given two ITS_LIVE Sentinel-1 image-pair products (i.e., NetCDF files), one is provided with all of the parameters needed to use Eq. (6) to calculate the map-projected velocities solely from LOS measurements. Figure 10 provides an example of this approach applied to ascending and descending Sentinel-1 image pairs both acquired on 20171226–20180101 in Region 3 (Table 3).

From Fig. 10a and d, it can be seen that the x and y velocities from the ascending pair are severely contaminated by the

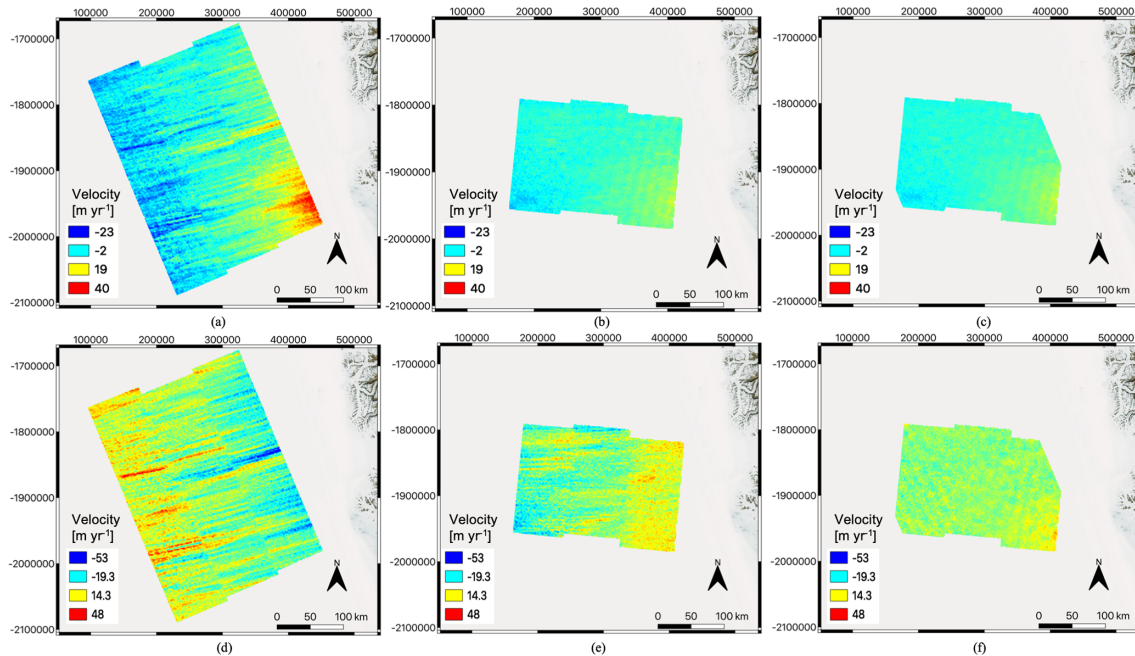


Figure 10. Ionosphere correction for ascending and descending acquisition geometry: (a) ascending x velocity, (b) descending x velocity, (c) ascending/descending combined x velocity, (d) ascending y velocity, (e) descending y velocity, (f) ascending/descending combined y velocity. The ascending/descending Sentinel-1 image pairs were both acquired on 20171226–20180101 in Region 3. Background: © Microsoft Bing Maps 2022.

ionosphere disturbance. Streaking is apparent in both x and y component velocities because the inclination of the ascending orbit projects some amount of the azimuth streaking into both coordinate directions. Figure 10b and e demonstrate the velocities for the descending pair. As the descending orbit has a small inclination, the ionosphere disturbance is only prominent in the y -direction velocity. Figure 10c and f show the final velocity fields obtained by combining the overlaps from both ascending and descending LOS image-pair measurements using Eq. (6). Using only LOS displacements significantly reduces the azimuth streaks. The uncertainty reduces from 8.6 m yr^{-1} (ascending) or 3.7 m yr^{-1} (descending) to 3.4 m yr^{-1} (by 9%–61%) for the x -direction velocity and from 12.9 m yr^{-1} (ascending) or 10.9 m yr^{-1} (descending) to 5.6 m yr^{-1} (by 49%–57%) for the y -direction velocity. These error seem more in line with what others are reporting in Table 1. Therefore, significant reductions in velocity error can be achieved, when provided with two ITS_LIVE Sentinel-1 image-pair products (i.e., NetCDF files only) acquired from ascending and descending geometry.

4 Validation

We validate the global ITS_LIVE Sentinel-1 image-pair products, against other publicly available products, for three typical locations: Jakobshavn Isbræ Glacier in Greenland (Sect. 4.1), Pine Island Glacier in the Antarctic (Sect. 4.2), and Malaspina Glacier in Alaska (Sect. 4.3).

4.1 Jakobshavn Isbræ Glacier

We first validate the ITS_LIVE Sentinel-1 image-pair products over the fast-flowing Jakobshavn Isbræ Glacier (69° N , 50° W ; Fig. 11), located in southwest Greenland. We compare the ITS_LIVE Sentinel-1 velocities to ITS_LIVE Version 2 image-pair products acquired from optical sensors (Landsat-8 and Sentinel-2) as well as the PROMICE ice velocities (Solgaard and Kusk, 2021), which are also produced from Sentinel-1 data using the offset tracking method (Solgaard et al., 2021). Jakobshavn Isbræ Glacier is the fastest glacier draining the ice sheet (Lemos et al., 2018). The glacier experienced successive break-up events during the late 1990s, and started to speed up afterwards, with the maximum velocity around 15 km yr^{-1} and an overall seasonal variability of 8 km yr^{-1} (Lemos et al., 2018). Jakobshavn Isbræ is the fastest moving glacier on Earth (Rial et al., 2009; Joughin et al., 2014) and thus serves as a challenging test case for validating the ITS_LIVE Sentinel-1 image-pair products.

As a qualitative comparison, we show the ITS_LIVE Sentinel-1 image-pair product (acquired on 20170404–20170410) along with the PROMICE product in Fig. 12. As the PROMICE product has a temporal resolution of 24 d, to maximize the temporal overlap, we used the PROMICE product that is temporally averaged between 20170323 and 20170416. The difference in grid spacing and effective spatial resolution is apparent between our ITS_LIVE Version 2 product (grid spacing of 120 m; effective spatial resolution

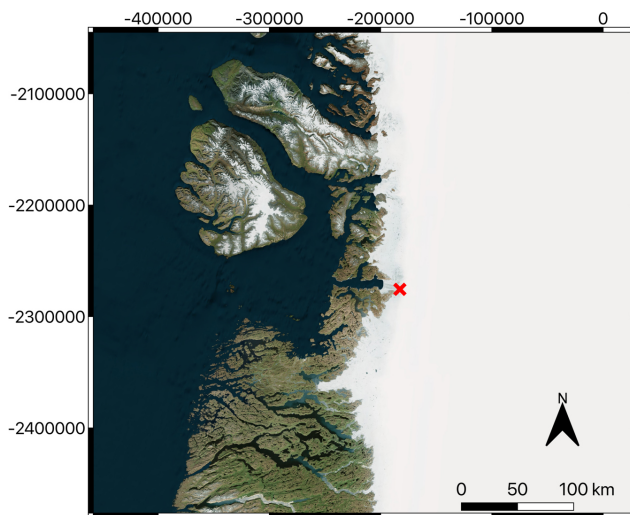


Figure 11. Optical image of the test site at the Jakobshavn Isbræ Glacier in Greenland, where the red cross marks the location of the fast-moving glacier outlet for the validation of the ITS_LIVE Sentinel-1 image-pair products. Background: © Microsoft Bing Maps 2022.

of 240 to 1920 m) and the PROMICE product (grid spacing of 500 m; effective spatial resolution of 800–900 m). It can also be seen from Fig. 12 that the PROMICE product has been smoothed/filtered spatially as well as averaged temporally by mosaicking all the 6 d and 12 d image-pair products within the 24 d temporal resolution window. This is exaggerated when looking at the site overview subfigure of Fig. 12b, where the northern part of the image shows strong azimuth streaks and the southern part has a discontinuity over stable surfaces. Due to this temporal mosaicking, there is a difference between the two products for the slowest moving velocities over stable surfaces, i.e., $\sim 20 \text{ m yr}^{-1}$. The fast-moving ice velocities (e.g., over the glacier outlet in the close-up of Fig. 12) look very similar between the two products, with improved coverage provided by the PROMICE temporal averaging.

We next compare time series generated from the ITS_LIVE Sentinel-1 image-pair product, the PROMICE product, and other ITS_LIVE Version 2 image-pair products acquired from Landsat-8 and Sentinel-2 sensors. The time series results and the error metrics are shown in Fig. 13, where all of the time series data were extracted at the location of the red cross marker (69.124° N , 49.496° W) in Fig. 11. It is shown in Fig. 13 that all of the products generally agree well, capturing the large interannual and seasonal velocity variation with a mean velocity around 10 km yr^{-1} and an overall dynamic range of 8 km yr^{-1} . The error metrics are summarized as such: R^2 of 0.97 and root mean square error (RMSE) of 314 m yr^{-1} (relative percentage of 3.7 %) between ITS_LIVE Sentinel-1 and ITS_LIVE Version 2 Landsat 8; R^2 of 0.97 and RMSE of 354 m yr^{-1} (relative percent-

age of 4.0 %) between ITS_LIVE Sentinel-1 and ITS_LIVE Version 2 Sentinel-2; R^2 of 0.95 and RMSE of 512 m yr^{-1} (relative percentage of 5.9 %) between ITS_LIVE Sentinel-1 and PROMICE. In generating the above error metrics, all of the other data products were resampled using the nearest neighbor method to the concurrent ITS_LIVE Sentinel-1 horizontal (time) axis, where 695 ITS_LIVE Sentinel-1, 534 ITS_LIVE Version 2 Landsat 8, 1380 ITS_LIVE Version 2 Sentinel-2 image-pair products as well as 157 PROMICE products were used. Note for each year of 2016–2022, there are periods that ITS_LIVE optical data are unavailable due to polar night. The inclusion of Sentinel-1 radar data in the ITS_LIVE record is critical to filling these gaps.

The v_x , v_y , and v uncertainty metrics of the ITS_LIVE Version 2 Sentinel-1 image-pair products shown in Fig. 13 are shown in Fig. 14 and are calculated using Eq. (3) as described at the end of Sect. 3.1.2. It is shown that an average uncertainty of 61 m yr^{-1} can be achieved while the error in v_x (35 m yr^{-1}) is smaller than that in v_y (71 m yr^{-1}) because of the coarser resolution in radar azimuth direction that mostly aligns with (thus impacts) the y -direction velocity. In generating the uncertainty metrics in Fig. 14, about 30 % of the 695 ITS_LIVE Sentinel-1 image-pair products that were exploited in Fig. 13 were not used here due to the known issue of wrong identification of stable surfaces over the fast-flowing Jakobshavn glacier outlet (flowing at a speed on the order of km yr^{-1}), which can in turn bias the uncertainty metric by a few 100s of meters per year. The alternative approach of calculating the uncertainty by using the slowest 25 % reference velocities as “stable surfaces” (Sect. 3.1.2) also tend to be problematic over such fast-flowing areas. Therefore, over fast-flowing glacierized regions, an accurate stable surface mask is required.

4.2 Pine Island Glacier

For validation over the Antarctic, we compare ITS_LIVE Sentinel-1 image-pair products over the Pine Island Glacier (75° S , 100° W ; Fig. 15) to ITS_LIVE Version 2 Landsat-8 and Sentinel-2 image-pair products, and to MEaSUREs Annual Antarctic Ice Velocity Maps, Version 1 (Mouginot et al., 2017a, b) that are generated using multiple SAR and optical satellite data (JAXA’s ALOS, ESA’s ENVISAT and Sentinel-1, CSA’s RADARSAT-1 and RADARSAT-2, DLR’s TerraSAR-X and TanDEM-X, as well as USGS’s Landsat-8). Pine Island Glacier is one of the fastest glaciers in the world and also a rapidly thinning and melting glacier, which is responsible for about 20 % of Antarctica Ice Sheet’s mass loss (Thomas et al., 2011; Favier et al., 2014; Nilsson et al., 2022). The glacier has thinned at an increasing rate over the past 40 years with the grounding line retreated by 10s of kilometres (Rignot et al., 2008; Favier et al., 2014).

As a qualitative comparison, we show the ITS_LIVE Sentinel-1 image-pair product (acquired on 20190110–20190116 and 20190122–20190128) along with the MEa-

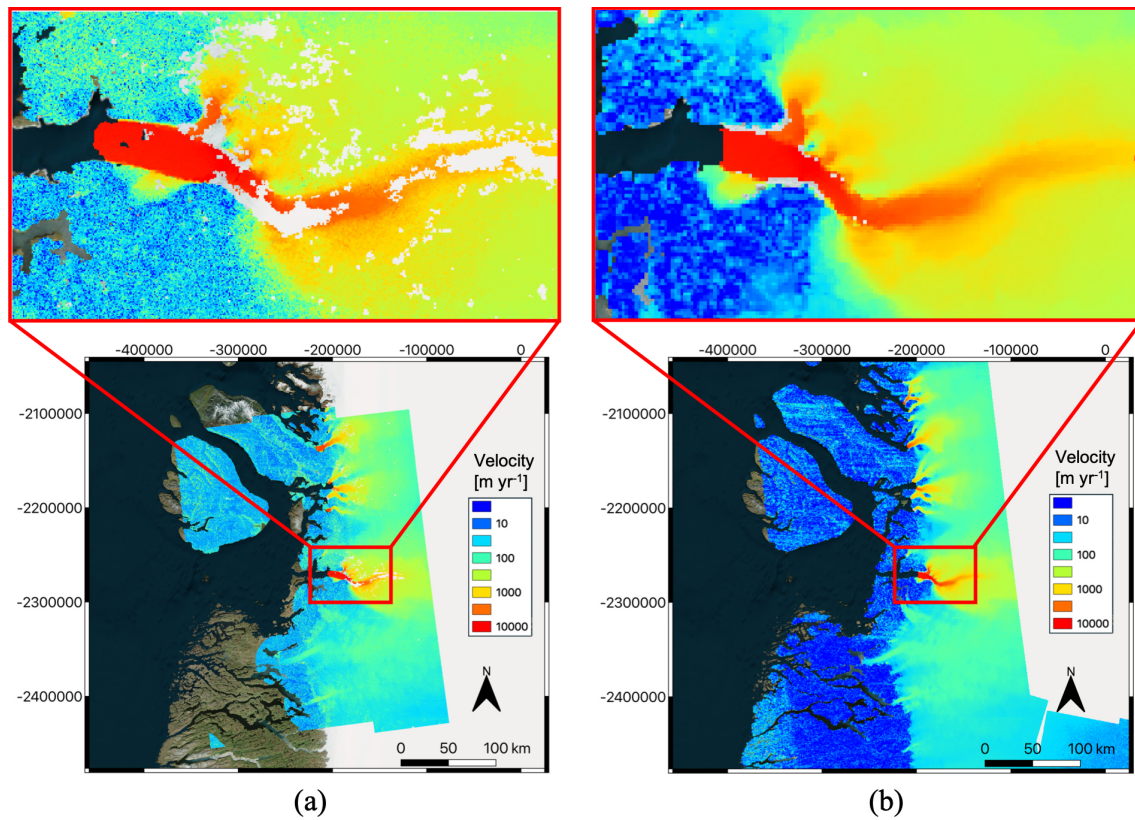


Figure 12. Comparison of (a) a single 120 m posting 6 d ITS_LIVE Sentinel-1 image pair (acquired on 20170404–20170410) to (b) the PROMICE 500 m posting 24 d averaged (20170323–20170416) product (b) for Jakobshavn Isbræ Glacier in Greenland. Background: © Microsoft Bing Maps 2022.

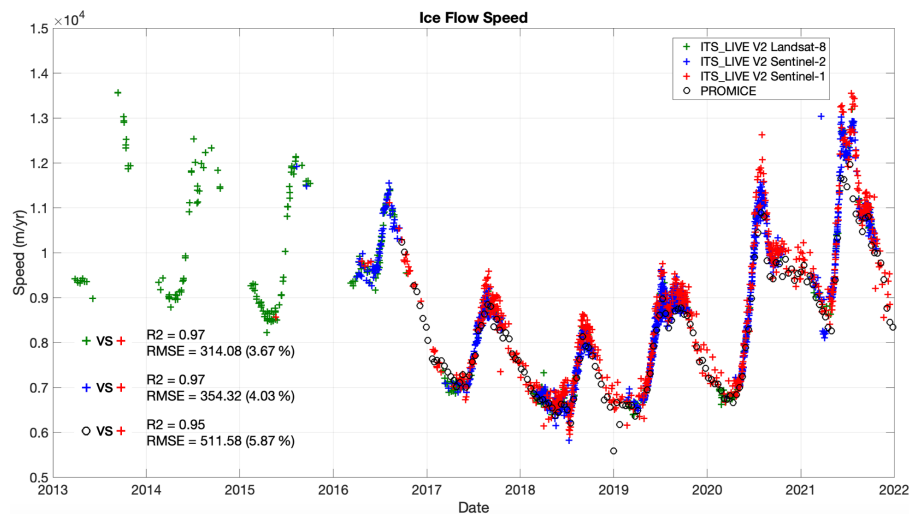


Figure 13. Time series of ITS_LIVE Sentinel-1 image-pair velocities, PROMICE velocities, and ITS_LIVE Version 2 Sentinel-2 and Landsat-8 products for the Jakobshavn Isbræ Glacier in Greenland at the location of the red cross marker (69.124° N, 49.496° W) in Fig. 11. The inter-product comparison metrics are also shown. The comparison includes 695 ITS_LIVE Sentinel-1, 534 ITS_LIVE Version 2 Landsat-8, 1380 ITS_LIVE Version 2 Sentinel-2 image-pair velocities as well as 157 PROMICE velocities. The time separation between repeat images ranges from 16 to 544 d for Landsat 8 and from 5 to 345 d for Sentinel-2 products.

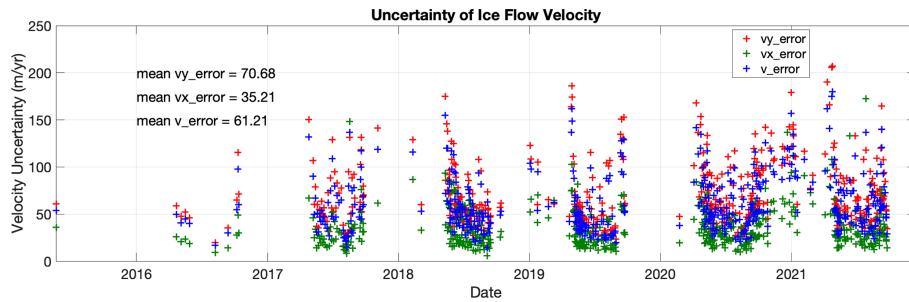


Figure 14. Uncertainty in ITS_LIVE Sentinel-1 image-pair velocities shown in Fig. 13 as provided in the product. Uncertainties of v_x , v_y and v are calculated according to Eq. (3).

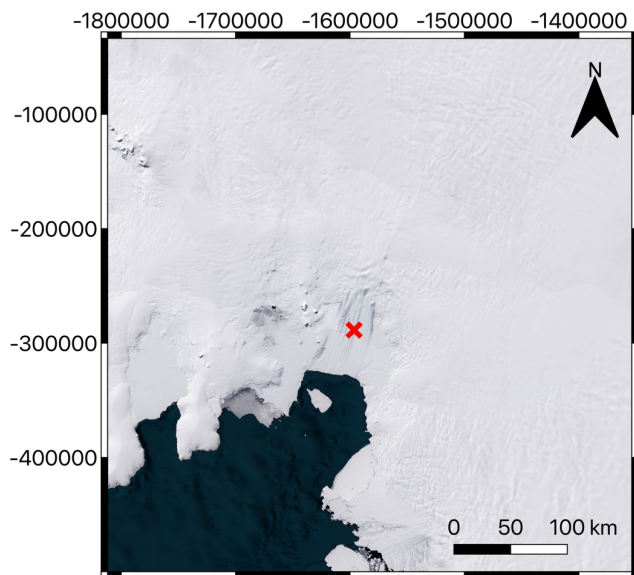


Figure 15. Optical image of the Pine Island Glacier in the Antarctic, where the red cross marks the location of the fast-moving glacier outlet that was used for the validation exercise. Background: © Microsoft Bing Maps 2022.

SUREs annual ice velocity product in Fig. 16. As the MEaSUREs Annual Antarctic Ice Velocity Maps have a temporal resolution of 1 year, we compare our data to the 2018–2019 mapping that is temporally averaged between July 2018 and June 2019. The difference in grid spacing can be noticed between the ITS_LIVE Version 2 product (grid spacing of 120 m) and the MEaSUREs annual product (grid spacing of 1000 m). It can also be seen from Fig. 16 that the MEaSUREs Annual Antarctic Ice Velocity Map has been spatially smoothed. The annual product is substantially better due to a significantly greater volume of data included in the annual average. However, the two products visually compare very well without noticeable difference for both slow-moving and fast-moving velocities.

Next, we show a cross-comparison between the ITS_LIVE Sentinel-1 image-pair product, the MEaSUREs Annual

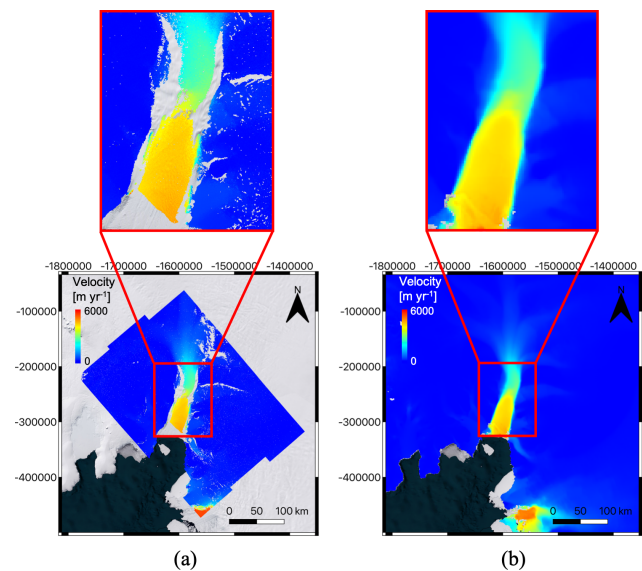


Figure 16. Comparison of (a) two 6 d (20190110–20190116 and 20190122–20190128) ITS_LIVE Sentinel-1 image-pair velocity (b) with the MEaSUREs Annual Antarctic Ice Velocity Maps averaged for the period of July 2018 to June 2019 over the Pine Island Glacier in the Antarctic. Background: © Microsoft Bing Maps 2022.

Antarctic Ice Velocity Maps, and ITS_LIVE Version 2 Landsat-8 and Sentinel-2 products. The comparison and the error metrics are shown in Fig. 17, where all of the time series data were extracted for the location shown by the red cross marker (75.14° S, 100.13° W) in Fig. 15. All of the products generally agree well, demonstrating both slow interannual and small seasonal velocity variation with the mean velocity around 4.35 km yr^{-1} and an overall dynamic range of 750 m yr^{-1} between 2013 and 2021. The error metrics are summarized as: R^2 of 0.87 and RMSE of 136 m yr^{-1} (relative percentage of 3.1 %) between ITS_LIVE Sentinel-1 and ITS_LIVE Version 2 Landsat 8; R^2 of 0.86 and RMSE of 94 m yr^{-1} (relative percentage of 2.1 %) between ITS_LIVE Sentinel-1 and ITS_LIVE Version 2 Sentinel-2; R^2 of 0.66 and RMSE of 120 m yr^{-1} (relative percentage of 2.8 %) be-

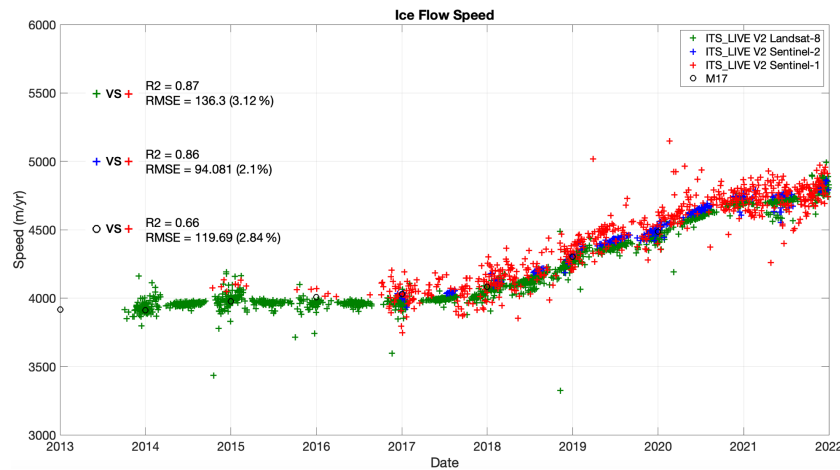


Figure 17. Time series of ITS_LIVE Sentinel-1 image-pair velocities, MEaSUREs Annual Antarctic Ice Velocity Maps (denoted as “M17”), and ITS_LIVE Version 2 Sentinel-2 and Landsat-8 products for Antarctica’s Pine Island Glacier for the location of the red cross marker (75.14° S, 100.13° W) in Fig. 15. The inter-product comparison metrics are also shown. The comparison includes 605 ITS_LIVE Sentinel-1, 1957 ITS_LIVE Version 2 Landsat 8, 223 ITS_LIVE Version 2 Sentinel-2 image-pair products as well as 16 MEaSUREs Annual Antarctic Ice Velocity Maps. The time separation between repeat images ranges from 16 to 544 d for Landsat 8 and 10 to 530 d for Sentinel-2 products.

tween ITS_LIVE Sentinel-1 and the MEaSUREs Annual Antarctic Ice Velocity Maps. In generating the above error metrics, all data products were resampled using the nearest neighbor method to the concurrent ITS_LIVE Sentinel-1 horizontal (time) axis, where 605 ITS_LIVE Sentinel-1, 1957 ITS_LIVE Version 2 Landsat 8, 223 ITS_LIVE Version 2 Sentinel-2 image-pair products as well as 16 MEaSUREs Annual Antarctic Ice Velocity Maps, were used.

Similar to Sect. 4.1, v_x , v_y , and v uncertainty metrics of the ITS_LIVE Version 2 Sentinel-1 image-pair products used in Fig. 17 are shown in Fig. 18 and are calculated using Eq. (3). For the selected point the velocity magnitude (v) has an average uncertainty of 67 m yr^{-1} while the uncertainty in v_x (52 m yr^{-1}) is slightly smaller than that in v_y (68 m yr^{-1}) due to the azimuth orientation that has slightly less projection onto the velocity in the x -direction for this location. Although Pine Island Glacier is on the other side of the planet from the Jakobshavn Isbræ Glacier (Sect. 4.1), the uncertainty metrics are very similar. This gives us confidence that the ITS_LIVE workflow produces consistent products for diverse regions of the globe.

4.3 Malaspina Glacier

Lastly, we validate the ITS_LIVE Sentinel-1 image-pair products for a mountain glacier, Malaspina Glacier (60° N, 140° W; Fig. 19), located in southeastern Alaska, using both ITS_LIVE Version 2 image-pair products acquired from optical sensors (Landsat-8 and Sentinel-2) as well as the FAU image-pair ice velocity products (RETREAT, 2021) that are globally available and were also created from Sentinel-1 data via the offset tracking method (Friedl et al., 2021). Malaspina glacier has the largest piedmont lobe of any temperate glacier

(Sauber et al., 2005; Rignot et al., 2013), which also serves as a good test case for validating the described methodology and the image-pair products over mountainous areas with high topographic relief.

As a qualitative comparison, we show the ITS_LIVE Sentinel-1 image-pair products (acquired on 20190225–20190303) alongside the FAU product in Fig. 20. FAU provides both monthly and annual mosaics and image-pair products with temporal baselines of 6 and 12 d. For this comparison we were able to locate the FAU product that uses the same Sentinel-1 images as the ITS_LIVE product. A difference in grid spacing and effective spatial resolution can be noticed between our ITS_LIVE Version 2 product (grid spacing of 120 m; effective spatial resolution 240–1920 m) and the FAU image-pair product (grid spacing of 200 m; effective spatial resolution 800–900 m). The FAU product appears to be spatially smoothed/filtered. This is due to FAU using a larger template window in offset tracking (thus suppressing some of the high-resolution details). Looking at the site overview subfigure of Fig. 20a and b, the FAU product also has less valid pixels over land but about the same coverage over glacier surfaces when compared to the ITS_LIVE product. Otherwise, both slow-flowing and fast-flowing velocity estimates visually compare very well between ITS_LIVE Sentinel-1 and FAU image-pair products.

Next, we show the comparison between the ITS_LIVE Sentinel-1, Landsat-8 and Sentinel-2 image-pair products and the FAU products. The time series results and the error metrics between various products are shown in Fig. 21, where all of the times series data were extracted at the location of the red cross marker (60.08° N, 140.47° W) in Fig. 19. It is shown in Fig. 21 that all of the products generally agree well, capturing the large interannual and seasonal velocity

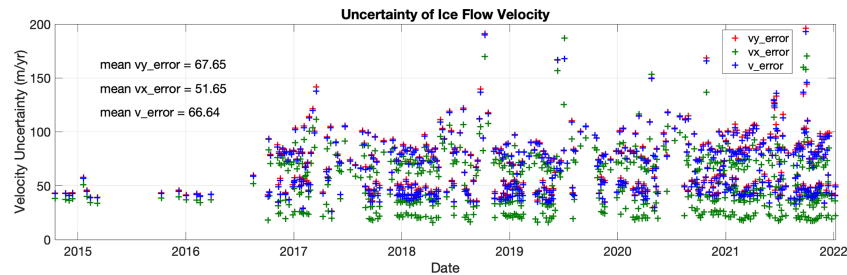


Figure 18. Uncertainty in ITS_LIVE Sentinel-1 image-pair velocities shown in Fig. 17 as provided in the product. The v_x , v_y and v uncertainties are calculated according to Eq. (3).

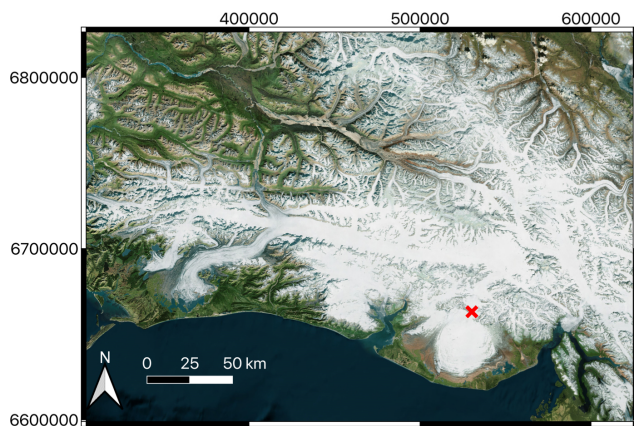


Figure 19. Optical image of the Malaspina Glacier in Alaska, where the red cross marks the location over the fast-moving glacier outlet for the validation of the velocity estimates against other products. Background: © Microsoft Bing Maps 2022.

variations with the mean velocity around 2 km yr^{-1} and an overall dynamic range of 3 km yr^{-1} , as well as a glacier surge after 2020. The error metrics are summarized as: R^2 of 0.92 and RMSE of 110 m yr^{-1} (relative percentage of 8.0 %) between ITS_LIVE Sentinel-1 and ITS_LIVE Version 2 Landsat 8; R^2 of 0.92 and RMSE of 130 m yr^{-1} (relative percentage of 9.1 %) between ITS_LIVE Sentinel-1 and ITS_LIVE Version 2 Sentinel-2; R^2 of 0.96 and RMSE of 147 m yr^{-1} (relative percentage of 9.4 %) between ITS_LIVE Sentinel-1 and FAU. In generating the above error metrics, all of the other data products were resampled using the nearest neighbor method to the concurrent ITS_LIVE Sentinel-1 horizontal (time) axis, where 715 ITS_LIVE Sentinel-1, 653 ITS_LIVE Version 2 Landsat 8, 1131 ITS_LIVE Version 2 Sentinel-2 image-pair products as well as 134 FAU products were used.

Similar to Sect. 4.1 and 4.2, v_x , v_y , and v uncertainty metrics of the ITS_LIVE Version 2 Sentinel-1 image-pair products shown in Fig. 21 are shown in Fig. 22 and are calculated using Eq. (3). It is shown that an average uncertainty of 58 m yr^{-1} can be achieved while the error in v_x (51 m yr^{-1}) is slightly smaller than that in v_y (61 m yr^{-1}) due to the azimuth

orientation. The uncertainty metrics for this mountain glacier are similar to those reported for Greenland and Antarctica.

Below we provide the implications of the data quality for smaller mountain glaciers. For global processing, autoRIFT uses square search chip sizes ranging from $240 \text{ m} \times 240 \text{ m}$ to $1920 \text{ m} \times 1920 \text{ m}$. Only a single velocity vector is returned for a single search chip. This means that when a single search chip covers a surface with steep spatial gradients in surface velocity (e.g., shear margins, glacier margins, nunataks), only a single velocity vector will be returned. The returned vector represents the displacement between features that provide maximum correlation. Rock often dominates the correlation for mixed search chips that contain rock. This can cause glacier velocities to be negatively biased for narrow valley glaciers and along shear margins. This same issue occurs for features that advect with the glacier (e.g., medial moraines) but present as stationary features. When a search chip samples these features the correlation can be dominated by the advecting moraine that appears as stationary. Lastly, Sentinel-1 is a side-looking SAR that is impacted by layover (i.e., multiple targets at the same range distance from the sensor are overlaid on each other) and line-of-sight shadowing effects (i.e., no targets appear at the side of a high mountain glacier facing away from the radar resulting in a lack of velocity data). Both of these issues are magnified in areas of high-relief where mountain glaciers are often located. These potential problems need to be further investigated and addressed when testing over small mountain glaciers in future work.

5 Code and data availability

The final release of MEaSUREs ITS_LIVE Sentinel-1 Image-Pair Glacier and Ice Sheet Surface Velocities: Version 2 ice velocity product (including image-pair maps, datacubes and mosaics) for Sentinel-1 (<https://doi.org/10.5067/0506KQLS6512>, Lei et al., 2022) as well as other optical sensors (Landsat-4/5/6/7/8 and Sentinel-2) can be found at the ITS_LIVE project website: <https://its-live.jpl.nasa.gov> (last access: 1 March 2022). The sample ITS_LIVE Sentinel-1 image-pair products for the

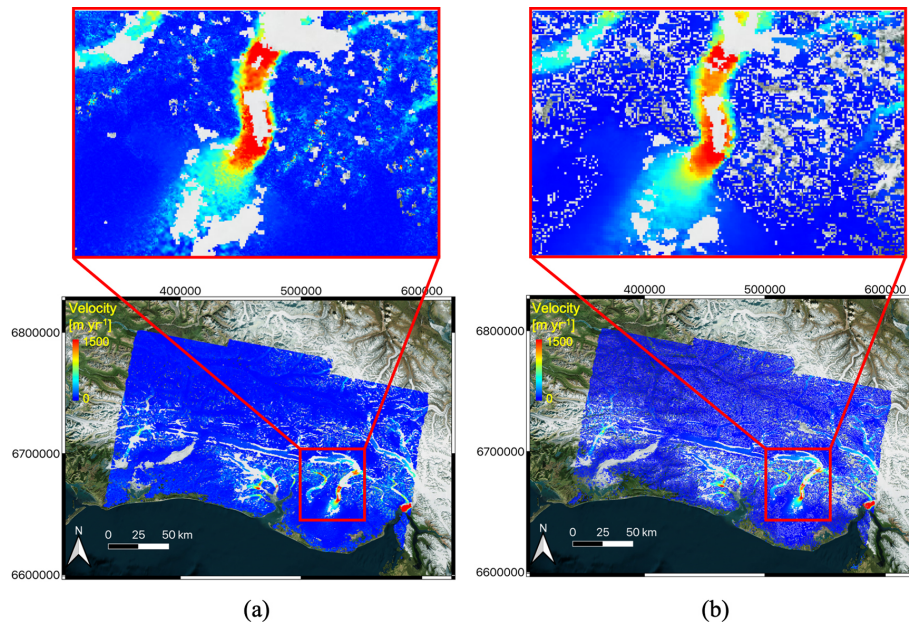


Figure 20. Comparison of the (a) ITS_LIVE Sentinel-1 image-pair product to the (b) FAU product over the test site at the Malaspina Glacier in Alaska. Both datasets are generated using Sentinel-1 images acquired on 20190225 and 20190303. Background: © Microsoft Bing Maps 2022.

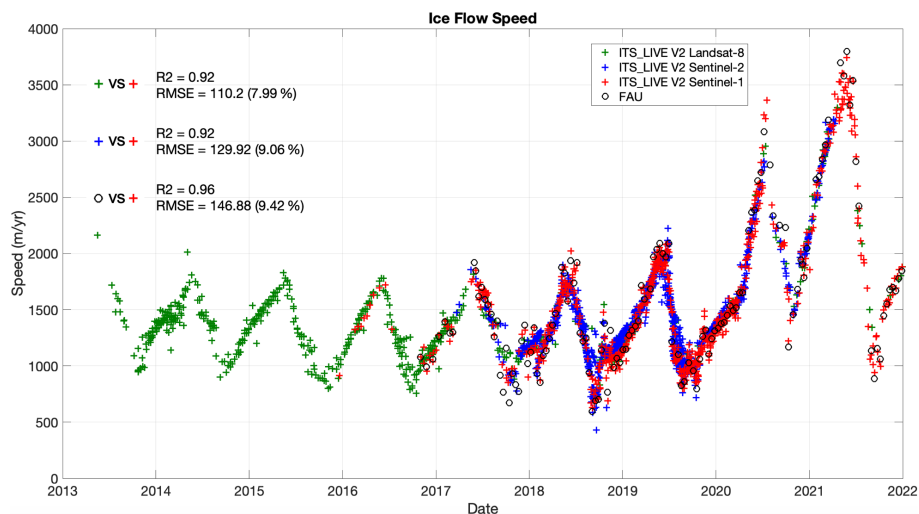


Figure 21. Time series of ITS_LIVE Sentinel-1 image-pair velocities, FAU velocities, and ITS_LIVE Version 2 Sentinel-2 and Landsat-8 products for Alaska's Malaspina Glacier for the location of the red cross marker (60.08° N, 140.47° W) in Fig. 19. The inter-product comparison metrics are also shown. The comparison includes 715 ITS_LIVE Sentinel-1, 653 ITS_LIVE Version 2 Landsat 8, 1131 ITS_LIVE Version 2 Sentinel-2 image-pair products as well as 134 FAU velocities. The time separation between repeat images ranges between 16 and 288 d for Landsat 8 and between 5 and 280 d for Sentinel 2 products.

21 Sentinel-1 image pairs used for methodology demonstration in this paper can be found at the following DOI: <https://doi.org/10.5281/zenodo.5606118> (Lei et al., 2021b). Regarding the input files for the global processing, we use the Copernicus DEM GLO-30 (<https://spacedata.copernicus.eu/web/cscda/dataset-details?articleId=394198>, last access: 1 March 2022) and ITS_LIVE Version 1 Landsat-8-derived

velocity mosaics (<https://its-live.jpl.nasa.gov>, last access: 1 March 2022) as the reference velocities for deriving all our ITS_LIVE Version 2 products. Regarding the cross-validation data, the PROMICE ice velocity products can be downloaded from <https://doi.org/10.22008/FK2/ZEGVXU> (Solgaard and Kusk, 2021). The FAU image-pair products can be found at <http://retreat.geographie.uni-erlangen.de>

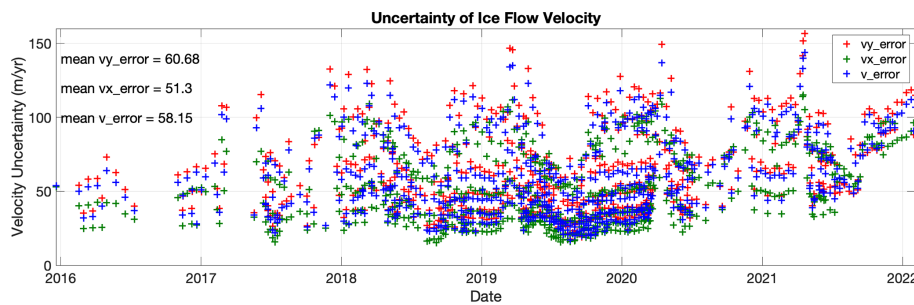


Figure 22. Uncertainty in ITS_LIVE Sentinel-1 image-pair velocities shown in Fig. 21 as provided in the products. The v_x , v_y and v uncertainties are calculated according to Eq. (3).

(last access: 1 March 2022, RETREAT, 2021; Friedl et al., 2021). The MEaSUREs Annual Antarctic Ice Velocity Maps can be found at <https://nsidc.org/data/NSIDC-0720/versions/1> (last access: 1 March 2022) (<https://doi.org/10.5067/9T4EPQXTJYW9>, Mouginot et al., 2017b).

6 Software tools

The MEaSUREs ITS_LIVE Sentinel-1 Image-Pair Glacier and Ice Sheet Surface Velocities: Version 2 are processed with the following software tools. First, ISCE Version 2.4+ (<https://github.com/isce-framework/isce2/releases>, last access: 1 March 2022; in particular the “topsApp” function) is used to preprocess the two Sentinel-1 images that form an image pair up to the step of “mergeBursts”, which results in co-registered SLC images. Then, *Geogrid/autorIFT* Version 1.4.0 (<https://doi.org/10.5281/zenodo.5643820>, Gardner et al., 2021) is used to generate the final NetCDF data product. For more details, the readers are referred to the help page of ISCE (<https://github.com/isce-framework/isce2>, last access: 1 March 2022), *Geogrid* (<https://github.com/leiyangleon/Geogrid>, last access: 1 March 2022) and *autorIFT* (<https://github.com/nasa-jpl/autorIFT>, last access: 1 March 2022).

7 Summary and conclusion

In this paper we describe the MEaSUREs ITS_LIVE Sentinel-1 Image-Pair Glacier and Ice Sheet Surface Velocities: Version 2 and the associated data-processing algorithms. The dataset is provided for all large glacierized regions. To demonstrate the data quality and algorithms we showcase 21 Sentinel-1 image pairs (Lei et al., 2021b) over 3 different sites in Greenland: 1 covering the Jakobshavn Isbræ Glacier to demonstrate algorithm performance in an area of fast flow and 2 other locations covering the interior of the ice sheet for calibration purposes.

We first summarized the ITS_LIVE Sentinel-1 image-pair products along with the data processing chain. Both the inputs and outputs of the processing chain are introduced in

detail. These image-pair products are generated by using the offset tracking processing chain that consists of two Python modules: *Geogrid* and *autorIFT*. In this work, the core offset tracking module, *autorIFT*, has been enhanced with a few techniques for better accuracy, processing efficiency and to accommodate overlapping search chips for finer resolution. Benchmark comparisons between *autorIFT* and *ampcor* show that *autorIFT* achieves improvement in efficiency of multiple orders of magnitude, while at the same time providing a $\sim 33\%$ reduction in uncertainty.

We then demonstrate approaches to reduce systematic error in Sentinel-1 image-pair products. First, the slant range/azimuth offset tracking results are calibrated for the subswath and full-swath-dependent geolocation bias for Sentinel-1A/B pairs. By investigating 11 pairs, the average pixel offset bias between subswaths 2 and 1 are -0.010 pixels in slant range and 0.019 pixels in azimuth, while the bias between subswaths 3 and 2 are -0.007 pixels in slant-range and 0.006 pixels in azimuth, which is referenced to an image pair with Sentinel-1A acquired prior to Sentinel-1B. These subswath offset bias estimates are then used as a static correction of the subswath-dependent geolocation error in each ITS_LIVE Sentinel-1 image-pair product. Following this, the full-swath-dependent geolocation bias is corrected in a dynamic way for each image pair by using stable surfaces (ice-free terrain and slow-moving ice $< 15 \text{ m yr}^{-1}$). Averaging 20 pairs, the calibrated velocity bias is -4.1 in slant range and -26.8 m yr^{-1} in azimuth, which is referenced to a 6 d Sentinel-1A/B pair with Sentinel-1A acquired prior to Sentinel-1B. A secondary method is tested with almost equivalent performance that uses the area of the slowest 25 % of the reference velocity whenever the image pair does not intersect the stable surface. Even in well-calibrated constellation missions, instrument-level differences that result in full-swath or subswath level offsets can exist. When Sentinel-1C and Sentinel-1D are launched, similar offset calibration exercises are needed before offsets generated from their imagery can be incorporated into ITS_LIVE-like projects and/or processing campaigns.

To reduce the impact of ionosphere-induced azimuth streaks, the product includes LOS parameters that support

x/y horizontal velocity inversion from two slant range measurements of both ascending and descending geometry. Using LOS measurements from two Sentinel-1 image pairs (one ascending and one descending) with a 6 d separation as well as the LOS parameter layers in the ITS_LIVE products, the uncertainty reduced is from 8.6 m yr^{-1} (ascending) or 3.7 (descending) to 3.4 m yr^{-1} (by 9%–61%) in the x -direction and from 12.9 m yr^{-1} (ascending) or 10.9 (descending) to 5.6 m yr^{-1} (by 49%–57%) in the y -direction. After applying the ionosphere correction approach in this paper, there is still some residual slowly varying trend due to ionosphere disturbance in the LOS offset tracking velocity estimates, which could be removed by referencing to known ground control points with zero velocity through a quadratic baseline fit (Mouginot et al., 2012; Joughin et al., 2017). As for future work, we plan to investigate the possibility of using a split-spectrum InSAR phase (Liang et al., 2019) to remove the slowly varying ionosphere trend from the SAR LOS offset-tracking result over high-coherence areas, and then using the ionosphere correction approach (Sect. 3.2) in this paper to derive velocity products solely from corrected SAR LOS measurements, which could help to mitigate the artifacts from ionosphere-caused slowly varying gradients (as well as azimuth streaks).

We further validated the ITS_LIVE Version 2 Sentinel-1 image-pair products (with 6-year time series of 1000s of epochs) over 3 test sites covering the globe: the Jakobshavn Isbræ Glacier in Greenland, the Pine Island Glacier in Antarctica, and the Malaspina Glacier in Alaska. Comparing with other similar products (PROMICE, FAU and MEaSUREs Annual Antarctic Ice Velocity Maps) and ITS_LIVE Version 2 products from optical sensors (Landsat-8 and Sentinel-2), we find an overall deviation between products around 100 m yr^{-1} over fast-flowing glacier outlets (where both mean velocity and dynamic variation are of the order of km yr^{-1}) and increases of up to $300\text{--}500 \text{ m yr}^{-1}$ (3%–6%) for the fastest Jakobshavn Isbræ Glacier. The uncertainty of the Sentinel-1 velocity products has been shown to be uniformly distributed around 60 m yr^{-1} for the velocity magnitude over the 3 regions investigated.

Other limitations and future work entail further improvements of the dynamic geolocation bias calibration when the stable surface mask is unavailable within the spatial extent of the image pairs, ionosphere-induced azimuth streak removal by using an a priori flow direction, and investigation and validation over small mountain glaciers. The approaches presented here are directly applicable to future radar satellite missions (e.g., the NASA-ISRO NISAR). It is our hope that by providing state of the art, low-latency glacier velocity products to the public we will accelerate the understanding of glacier and ice sheet response to changes in oceans and the atmosphere.

Author contributions. ASG conceived the ITS_LIVE project. ASG and PA provided the high-level designs of the Sentinel-1 ice velocity processing and data product. YL, ASG and PA developed the processing software (*autoRIFT/Geogrid*), designed cal/val tests, and set up the format and layers of the final NetCDF product. YL prepared the manuscript with contributions from all co-authors.

Competing interests. The contact author has declared that none of the authors has any competing interests.

Disclaimer. Publisher's note: Copernicus Publications remains neutral with regard to jurisdictional claims in published maps and institutional affiliations.

Acknowledgements. This effort was funded by the NASA MEaSUREs program in contribution to the Inter-mission Time Series of Land Ice Velocity and Elevation (ITS_LIVE) project (<https://its-live.jpl.nasa.gov>, last access: 1 March 2022) and through Alex Gardner's participation in the NASA NISAR Science Team.

Financial support. This effort was funded by the NASA MEaSUREs program in contribution to the Inter-Mission Time Series of Land Ice Velocity and Elevation (ITS_LIVE) project (<https://its-live.jpl.nasa.gov/>, last access: 1 March 2022) and through Alex Gardner's participation in the NASA NISAR Science Team. Research conducted at the Jet Propulsion Laboratory, California Institute of Technology under contract with the National Aeronautics and Space Administration.

Review statement. This paper was edited by David Carlson and reviewed by Saurabh Vijay and two anonymous referees.

References

- Andersen, J. K., Kusk, A., Boncori, J. P. M., Hvidberg, C. S., and Grinsted, A.: Improved ice velocity measurements with Sentinel-1 TOPS interferometry, *Remote Sensing*, 12, 2014, <https://doi.org/10.3390/rs12122014>, 2020.
- Bamber, J. L. and Rivera, A.: A review of remote sensing methods for glacier mass balance determination, *Global Planet. Change*, 59, 138–148, 2007.
- Bechor, N. B. and Zebker, H. A.: Measuring two-dimensional movements using a single InSAR pair, *Geophys. Res. Lett.*, 33, L16311, <https://doi.org/10.1029/2006GL026883>, 2006.
- Bindschadler, R. A. and Scambos, T. A.: Satellite-image-derived velocity field of an Antarctic ice stream, *Science*, 252, 242–246, 1991.
- Boncori, J. P. M., Langer Andersen, M., Dall, J., Kusk, A., Kamstra, M., Bech Andersen, S., Bechor, N., Bevan, S., Bignami, C., Gourmelen, N., and Joughin, I.: Intercomparison and validation of SAR-based ice velocity measurement techniques within the Greenland Ice Sheet CCI project, *Remote Sensing*, 10, 929, <https://doi.org/10.3390/rs10060929>, 2018.

- Dehecq, A., Gourmelen, N., and Trouvé, E.: Deriving large-scale glacier velocities from a complete satellite archive: Application to the Pamir–Karakoram–Himalaya, *Remote Sens. Environ.*, 162, 55–66, 2015.
- de Lange, R., Luckman, A., and Murray, T.: Improvement of satellite radar feature tracking for ice velocity derivation by spatial frequency filtering, *IEEE T. Geosci. Remote*, 45, 2309–2318, 2007.
- Derkacheva, A., Mouginot, J., Millan, R., Maier, N., and Gillet-Chaulet, F.: Data Reduction Using Statistical and Regression Approaches for Ice Velocity Derived by Landsat-8, Sentinel-1 and Sentinel-2, *Remote Sensing*, 12, 1935, <https://doi.org/10.3390/rs12121935>, 2020.
- De Zan, F. and Garmieri, A. M.: TOPSAR: Terrain observation by progressive scans, *IEEE T. Geosci. Remote*, 44, 2352–2360, 2006.
- Fahnestock, M., Bindschadler, R., Kwok, R., and Jezek, K.: Greenland ice sheet surface properties and ice dynamics from ERS-1 SAR imagery, *Science*, 262, 1530–1534, 1993.
- Fahnestock, M., Scambos, T., Moon, T., Gardner, A., Haran, T., and Klinger, M.: Rapid large-area mapping of ice flow using Landsat 8, *Remote Sens. Environ.*, 185, 84–94, 2016.
- Farinotti, D., Huss, M., Fürst, J. J., Landmann, J., Machguth, H., Maussion, F., and Pandit, A.: A consensus estimate for the ice thickness distribution of all glaciers on Earth, *Nat. Geosci.*, 12, 168–173, 2019.
- Favier, L., Durand, G., Cornford, S. L., Gudmundsson, G. H., Gagliardini, O., Gillet-Chaulet, F., Zwinger, T., Payne, A. J., and Le Brocq, A. M.: Retreat of Pine Island Glacier controlled by marine ice-sheet instability, *Nat. Clim. Change*, 4, 117–121, 2014.
- Friedl, P., Seehaus, T., and Braun, M.: Global time series and temporal mosaics of glacier surface velocities derived from Sentinel-1 data, *Earth Syst. Sci. Data*, 13, 4653–4675, <https://doi.org/10.5194/essd-13-4653-2021>, 2021.
- Frolich, R. M. and Doake, C. S. M.: Synthetic aperture radar interferometry over Rutford Ice Stream and Carlson Inlet, Antarctica, *J. Glaciol.*, 44, 77–92, 1998.
- Gardner, A. S., Moholdt, G., Scambos, T., Fahnestock, M., Ligtenberg, S., van den Broeke, M., and Nilsson, J.: Increased West Antarctic and unchanged East Antarctic ice discharge over the last 7 years, *The Cryosphere*, 12, 521–547, <https://doi.org/10.5194/tc-12-521-2018>, 2018.
- Gardner, A. S., Fahnestock, M. A., and Scambos, T. A.: ITS_LIVE Regional Glacier and Ice Sheet Surface Velocities, National Snow and Ice Data Center [data set], <https://doi.org/10.5067/6II6VW8LLWJ7>, 2019.
- Gardner, A. S., Lei, Y., and Agram, P.: autoRIFT (autonomous Repeat Image Feature Tracking) (1.4.0), Zenodo [code], <https://doi.org/10.5281/zenodo.5643820>, 2021.
- Gisinger, C., Schubert, A., Breit, H., Garthwaite, M., Balss, U., Willberg, M., Small, D., Eineder, M., and Miranda, N.: In-depth verification of Sentinel-1 and TerraSAR-X geolocation accuracy using the Australian corner reflector array, *IEEE T. Geosci. Remote*, 59, 1154–1181, 2020.
- Goldstein, R. M., Engelhardt, H., Kamb, B., and Frolich, R. M.: Satellite radar interferometry for monitoring ice sheet motion: application to an Antarctic ice stream, *Science*, 262, 1525–1530, 1993.
- Gourmelen, N., Kim, S. W., Shepherd, A., Park, J. W., Sundal, A. V., Björnsson, H., and Pálsson, F.: Ice velocity determined using conventional and multiple-aperture InSAR, *Earth Planet. Sc. Lett.*, 307, 156–160, 2011.
- Gray, A. L., Mattar, K. E., Vachon, P. W., Bindschadler, R., Jezek, K. C., Forster, R., and Crawford, J. P.: InSAR results from the RADARSAT Antarctic Mapping Mission data: estimation of glacier motion using a simple registration procedure, in: IGARSS'98. Sensing and Managing the Environment, 1998 IEEE International Geoscience and Remote Sensing, Symposium Proceedings, Cat. No. 98CH36174, Vol. 3, 1638–1640, IEEE July, 1998.
- Gray, A. L., Mattar, K. E., and Sofko, G.: Influence of ionospheric electron density fluctuations on satellite radar interferometry, *Geophys. Res. Lett.*, 27, 1451–1454, 2000.
- Greene, C. A., Gardner, A. S., and Andrews, L. C.: Detecting seasonal ice dynamics in satellite images, *The Cryosphere*, 14, 4365–4378, <https://doi.org/10.5194/tc-14-4365-2020>, 2020.
- Howat, I. M., Negrete, A., and Smith, B. E.: The Greenland Ice Mapping Project (GIMP) land classification and surface elevation data sets, *The Cryosphere*, 8, 1509–1518, <https://doi.org/10.5194/tc-8-1509-2014>, 2014.
- Howat, I., Negrete, A., and Smith, B.: MEaSURES Greenland Ice Mapping Project (GIMP) Digital Elevation Model, Version 1; NASA National Snow and Ice Data Center Distributed Active Archive Center, Boulder, CO, USA [data set], <https://doi.org/10.5067/NV34YUIXLP9W>, 2015.
- IPCC AR6: Sixth Assessment Report, <https://www.ipcc.ch/assessment-report/ar6/>, last access: 22 October 2021.
- Jiao, Y., Morton, Y. T., Taylor, S., and Pelgrum, W.: Characterization of high-latitude ionospheric scintillation of GPS signals, *Radio Sci.*, 48, 698–708, 2013.
- Joughin, I.: Ice-sheet velocity mapping: a combined interferometric and speckle-tracking approach, *Ann. Glaciol.*, 34, 195–201, 2002.
- Joughin, I.: MEaSURES Greenland Annual Ice Sheet Velocity Mosaics from SAR and Landsat, Version 2, NASA National Snow and Ice Data Center Distributed Active Archive Center, Boulder, Colorado USA [data set], <https://doi.org/10.5067/TZZDYD94IMJB>, 2020a.
- Joughin, I.: MEaSURES Greenland Monthly Ice Sheet Velocity Mosaics from SAR and Landsat, Version 2, NASA National Snow and Ice Data Center Distributed Active Archive Center, Boulder, Colorado USA [data set], <https://doi.org/10.5067/11MJZGPBK3ZF>, 2020b.
- Joughin, I. R., Winebrenner, D. P., and Fahnestock, M. A.: Observations of ice-sheet motion in Greenland using satellite radar interferometry, *Geophys. Res. Lett.*, 22, 571–574, 1995.
- Joughin, I. R., Kwok, R., and Fahnestock, M. A.: Interferometric estimation of three-dimensional ice-flow using ascending and descending passes, *IEEE T. Geosci. Remote*, 36, 25–37, 1998.
- Joughin, I., Gray, L., Bindschadler, R., Price, S., Morse, D., Hulbe, C., Mattar, K., and Werner, C.: Tributaries of West Antarctic ice streams revealed by RADARSAT interferometry, *Science*, 286, 283–286, 1999.
- Joughin, I., Smith, B. E., Howat, I. M., Scambos, T., and Moon, T.: Greenland flow variability from ice-sheet-wide velocity mapping, *J. Glaciol.*, 56, 415–430, 2010.

- Joughin, I., Smith, B. E., Shean, D. E., and Floricioiu, D.: Brief Communication: Further summer speedup of Jakobshavn Isbræ, *The Cryosphere*, 8, 209–214, <https://doi.org/10.5194/tc-8-209-2014>, 2014.
- Joughin, I., Smith, B., Howat, I., and Scambos, T.: MEaSUREs Greenland Ice Sheet Velocity Map from InSAR Data, Version 2, NASA National Snow and Ice Data Center Distributed Active Archive Center, Boulder, Colorado USA [data set], <https://doi.org/10.5067/OC7B04ZM9G6Q>, 2015.
- Joughin, I., Smith, B., Howat, I., and Scambos, T.: MEaSUREs Multi-year Greenland Ice Sheet Velocity Mosaic, Version 1; NASA National Snow and Ice Data Center Distributed Active Archive Center, Boulder, CO, USA [data set], <https://doi.org/10.5067/QUA5Q9SVMSJG>, 2016.
- Joughin, I. A. N., Smith, B. E., and Howat, I. M.: A complete map of Greenland ice velocity derived from satellite data collected over 20 years, *J. Glaciol.*, 64, 1–11, <https://doi.org/10.1017/jog.2017.73>, 2017.
- Joughin, I., Smith, B. E., and Howat, I.: Greenland Ice Mapping Project: ice flow velocity variation at sub-monthly to decadal timescales, *The Cryosphere*, 12, 2211–2227, <https://doi.org/10.5194/tc-12-2211-2018>, 2018.
- Kääb, A., Winsvold, S. H., Altena, B., Nuth, C., Nagler, T., and Wuite, J.: Glacier remote sensing using Sentinel-2. Part I: Radiometric and geometric performance, and application to ice velocity, *Remote Sensing*, 8, 598, <https://doi.org/10.3390/rs8070598>, 2016.
- Kusk, A., Boncori, J. P. M., and Dall, J.: An automated system for ice velocity measurement from SAR, in: EUSAR 2018; 12th European Conference on Synthetic Aperture Radar, VDE, June, 1–4, 2018.
- Lei, Y., Gardner, A., and Agram, P.: Autonomous Repeat Image Feature Tracking (autoRIFT) and Its Application for Tracking Ice Displacement, *Remote Sens.* 13, 749, <https://doi.org/10.3390/rs13040749>, 2021a.
- Lei, Y., Gardner, A., and Agram, P.: MEaSUREs ITS_LIVE Sentinel-1 Image-Pair Glacier and Ice Sheet Surface Velocities: Version 2 (Greenland sample products), Zenodo [data set], <https://doi.org/10.5281/zenodo.5606118>, 2021b.
- Lei, Y., Gardner, A. S., Kennedy, J., Fahnestock, M., Agram, P., Liukis, M., Greene, C., Johnston, A., Lopez, L., and Scambos, T.: MEaSUREs ITS_LIVE Sentinel-1 Image-Pair Glacier and Ice Sheet Surface Velocities, Version 2, National Snow and Ice Data Center [data set], <https://doi.org/10.5067/0506KQLS6512>, 2022.
- Lemos, A., Shepherd, A., McMillan, M., Hogg, A. E., Hatton, E., and Joughin, I.: Ice velocity of Jakobshavn Isbræ, Petermann Glacier, Nioghalvfjærdsfjorden, and Zachariæ Isstrøm, 2015–2017, from Sentinel 1-a/b SAR imagery, *The Cryosphere*, 12, 2087–2097, <https://doi.org/10.5194/tc-12-2087-2018>, 2018.
- Liang, C., Agram, P., Simons, M., and Fielding, E. J.: Ionospheric correction of InSAR time series analysis of C-band Sentinel-1 TOPS data, *IEEE T. Geosci. Remote.* 57, 6755–6773, 2019.
- Liao, H., Meyer, F. J., Scheuchl, B., Mouginot, J., Joughin, I., and Rignot, E.: Ionospheric correction of InSAR data for accurate ice velocity measurement at polar regions, *Remote Sens. Environ.*, 209, 166–180, 2018.
- Meyer, F., Bamler, R., Jakowski, N., and Fritz, T.: The potential of low-frequency SAR systems for mapping ionospheric TEC distributions, *IEEE Geosci. Remote S.*, 3, 560–564, 2006.
- Michel, R. and Rignot, E.: Flow of Glacier Moreno, Argentina, from repeat-pass Shuttle Imaging Radar images: comparison of the phase correlation method with radar interferometry, *J. Glaciol.*, 45, 93–100, 1999.
- Miles, K. E., Willis, I. C., Benedek, C. L., Williamson, A. G., and Tedesco, M.: Toward monitoring surface and sub-surface lakes on the Greenland ice sheet using Sentinel-1 SAR and Landsat-8 OLI imagery, *Front. Earth Sci.*, 5, 58, <https://doi.org/10.3389/feart.2017.00058>, 2017.
- Millan, R., Mouginot, J., Rabatel, A., Jeong, S., Cusicanqui, D., Derkacheva, A., and Chekki, M.: Mapping surface flow velocity of glaciers at regional scale using a multiple sensors approach, *Remote Sensing*, 11, 2498, <https://doi.org/10.3390/rs11212498>, 2019.
- Minchew, B. M., Simons, M., Riel, B., and Milillo, P.: Tidally induced variations in vertical and horizontal motion on Rutford Ice Stream, West Antarctica, inferred from remotely sensed observations, *J. Geophys. Res.-Earth*, 122, 167–190, 2017.
- Minowa, M., Schaefer, M., Sugiyama, S., Sakakibara, D., and Skvarca, P.: Frontal ablation and mass loss of the Patagonian icefields, *Earth Planet. Sc. Lett.*, 561, 116811, <https://doi.org/10.1016/j.epsl.2021.116811>, 2021.
- Miranda, N., Meadows, P., Piantanida, R., Recchia, A., Small, D., Schubert, A., Vincent, P., Geudtner, D., Navas-Traver, I., and Vega, F. C.: The Sentinel-1 constellation mission performance, in: 2017 IEEE International Geoscience and Remote Sensing Symposium (IGARSS), IEEE, July, 5541–5544, 2017.
- Mouginot, J., Scheuchl, B., and Rignot, E.: Mapping of ice motion in Antarctica using synthetic-aperture radar data, *Remote Sensing*, 4, 2753–2767, 2012.
- Mouginot, J., Rignot, E., Scheuchl, B., and Millan, R.: Comprehensive annual ice sheet velocity mapping using Landsat-8, Sentinel-1, and RADARSAT-2 data, *Remote Sensing*, 9, 364, <https://doi.org/10.3390/rs9040364>, 2017a.
- Mouginot, J., Scheuchl, B., and Rignot, E.: MEaSUREs Annual Antarctic Ice Velocity Maps, Version 1, NASA National Snow and Ice Data Center Distributed Active Archive Center, Boulder, Colorado USA [data set], <https://doi.org/10.5067/9T4EPQXTJYW9>, 2017b.
- Mouginot, J., Rignot, E., and Scheuchl, B.: Continent-wide, interferometric SAR phase, mapping of Antarctic ice velocity, *Geophys. Res. Lett.*, 46, 9710–9718, 2019a.
- Mouginot, J., Rignot, E., Scheuchl, B., Wood, M., and Millan, R.: Annual Ice Velocity of the Greenland Ice Sheet (2010–2017), Dryad [data set], <https://doi.org/10.7280/D11H3X>, 2019b.
- Nagler, T., Rott, H., Hetzenecker, M., Scharrer, K., Magnússon, E., Floricioiu, D., and Notarnicola, C.: Retrieval of 3D-glacier movement by high resolution X-band SAR data, in: 2012 IEEE International Geoscience and Remote Sensing Symposium, IEEE, July, 3233–3236, 2012.
- Nagler, T., Rott, H., Hetzenecker, M., Wuite, J., and Potin, P.: The Sentinel-1 mission: New opportunities for ice sheet observations, *Remote Sensing*, 7, 9371–9389, 2015.
- Nagy, T. and Andreassen, L. M.: Glacier surface velocity mapping with Sentinel-2 imagery in Norway, *Rapport, engelsknr* 37, 2019.
- Nilsson, J., Gardner, A. S., and Paolo, F. S.: Elevation change of the Antarctic Ice Sheet: 1985 to 2020, *Earth Syst. Sci. Data*, 14, 3573–3598, <https://doi.org/10.5194/essd-14-3573-2022>, 2022.

- Prats-Iraola, P., Nannini, M., Scheiber, R., De Zan, F., Wollstadt, S., Minati, F., Vecchioli, F., Costantini, M., Borgstrom, S., De Martino, P., and Siniscalchi, V.: Sentinel-1 assessment of the interferometric wide-swath mode, in: 2015 IEEE international geoscience and remote sensing symposium (IGARSS), IEEE, July, 5247–5251, 2015.
- RETREAT: Ice surface velocities derived from Sentinel-1, Version 1, FAU [data set], <http://retreat.geographie.uni-erlangen.de>, (last access: 1 March 2022), 2021.
- Rial, J. A., Tang, C., and Steffen, K.: Glacial rumblings from Jakobshavn ice stream, Greenland, *J. Glaciol.*, 55, 389–399, 2009.
- Rignot, E. and Mouginot, J.: Ice flow in Greenland for the international polar year 2008–2009, *Geophys. Res. Lett.*, 39, L11501, <https://doi.org/10.1029/2012GL051634>, 2012.
- Rignot, E., Jezek, K. C., and Sohn, H. G.: Ice flow dynamics of the Greenland ice sheet from SAR interferometry, *Geophys. Res. Lett.*, 22, 575–578, 1995.
- Rignot, E., Bamber, J. L., Van Den Broeke, M. R., Davis, C., Li, Y., Van De Berg, W. J., and Van Meijgaard, E.: Recent Antarctic ice mass loss from radar interferometry and regional climate modelling, *Nat. Geosci.*, 1, 106–110, 2008.
- Rignot, E., Mouginot, J., Larsen, C. F., Gim, Y., and Kirchner, D.: Low-frequency radar sounding of temperate ice masses in Southern Alaska, *Geophys. Res. Lett.*, 40, 5399–5405, 2013.
- Rignot, E., Mouginot, J., and Scheuchl, B.: MEaSURES InSAR-Based Antarctica Ice Velocity Map, Version 2, NASA National Snow and Ice Data Center Distributed Active Archive Center, Boulder, Colorado USA [data set], <https://doi.org/10.5067/D7GK8F5J8M8R>, 2017.
- Riveros, N., Euillades, L., Euillades, P., Moreiras, S., and Balbarani, S.: Offset tracking procedure applied to high resolution SAR data on Viedma Glacier, Patagonian Andes, Argentina, *Adv. Geosci.*, 35, 7–13, <https://doi.org/10.5194/adgeo-35-7-2013>, 2013.
- Sánchez-Gómez, P. and Navarro, F. J.: Glacier surface velocity retrieval using D-InSAR and offset tracking techniques applied to ascending and descending passes of Sentinel-1 data for southern Ellesmere ice caps, Canadian Arctic, *Remote Sensing*, 9, 442, <https://doi.org/10.3390/rs9050442>, 2017.
- Sauber, J., Molnia, B., Carabajal, C., Luthcke, S., and Muskett, R.: Ice elevations and surface change on the Malaspina Glacier, Alaska, *Geophys. Res. Lett.*, 32, L23S01, <https://doi.org/10.1029/2005GL023943>, 2005.
- Schubert, A., Miranda, N., Geudtner, D., and Small, D.: Sentinel-1A/B combined product geolocation accuracy, *Remote sensing*, 9, 607, <https://doi.org/10.3390/rs9060607>, 2017.
- Solgaard, A. M. and Kusk, A.: Greenland Ice Velocity from Sentinel-1 Edition 2, V11, GEUS Dataverse [data set], <https://doi.org/10.22008/FK2/ZEGVXU>, 2021.
- Solgaard, A., Kusk, A., Merryman Boncori, J. P., Dall, J., Mankoff, K. D., Ahlstrøm, A. P., Andersen, S. B., Citterio, M., Karlsson, N. B., Kjeldsen, K. K., Korsgaard, N. J., Larsen, S. H., and Fausto, R. S.: Greenland ice velocity maps from the PROMICE project, *Earth Syst. Sci. Data*, 13, 3491–3512, <https://doi.org/10.5194/essd-13-3491-2021>, 2021.
- Stein, A. N., Huertas, A., and Matthies, L.: Attenuating stereo pixel-locking via affine window adaptation, in: Proceedings 2006 IEEE International Conference on Robotics and Automation, 2006, ICRA 2006, IEEE, May, 914–921, <https://doi.org/10.1109/ROBOT.2006.1641826>, 2006.
- Strozzi, T., Luckman, A., Murray, T., Wegmüller, U., and Werner, C. L.: Glacier motion estimation using SAR offset-tracking procedures, *IEEE T. Geosci. Remote*, 40, 2384–2391, 2002.
- Strozzi, T., Kouraev, A., Wiesmann, A., Wegmüller, U., Sharov, A., and Werner, C.: Estimation of Arctic glacier motion with satellite L-band SAR data, *Remote Sens. Environ.*, 112, 636–645, 2008.
- Thomas, R., Frederick, E., Li, J., Krabill, W., Manizade, S., Paden, J., Sonntag, J., Swift, R., and Yungel, J.: Accelerating ice loss from the fastest Greenland and Antarctic glaciers, *Geophys. Res. Lett.*, 38, L10502, <https://doi.org/10.1029/2011GL047304>, 2011.
- Yu, J., Liu, H., Jezek, K. C., Warner, R. C., and Wen, J.: Analysis of velocity field, mass balance, and basal melt of the Lambert Glacier–Amery Ice Shelf system by incorporating Radarsat SAR interferometry and ICESat laser altimetry measurements, *J. Geophys. Res.-Sol. Ea.*, 115, B11102, <https://doi.org/10.1029/2010JB007456>, 2010.
- Zhang, Y., Fattahi, H., Pi, X., Rosen, P., Simons, M., Agram, P., and Aoki, Y.: Range Geolocation Accuracy of C/L-band SAR and its Implications for Operational Stack Coregistration, *IEEE T. Geosci. Remote*, 60, 5227219, <https://doi.org/10.1109/TGRS.2022.3168509>, 2022.